

Large Environments Reveal the Statistical Structure Governing Hippocampal Representations

P. Dylan Rich^{1,2*}, Hua-Peng Liaw¹, Albert K. Lee^{1*}

¹Howard Hughes Medical Institute, Janelia Farm Research Campus, Ashburn, VA 20147, USA.

²Department of Psychology, University of Cambridge, Downing Street, Cambridge CB2 3EB, UK.

*To whom correspondence should be addressed. Email: richp@janelia.hhmi.org; leea@janelia.hhmi.org.

The rules governing the formation of spatial maps in the hippocampus have not been determined. We recorded hippocampal neurons from rats exploring a previously unencountered 48-meter-long track, exposing the large-scale structure of place field activity. Single-cell and population activity was well-described by a two-parameter stochastic model. Individual neurons had their own characteristic propensity for forming fields randomly along the track, with some cells expressing many fields and many exhibiting few or none. Due to the particular distribution of propensities across cells, the number of neurons with fields scaled logarithmically with track length over a wide, ethological range. These features constrain hippocampal memory mechanisms, may allow efficient encoding of environments and experiences of vastly different extents and durations, and could reflect general principles of population coding.

One Sentence Summary: The hippocampal representation of space scales logarithmically with environment size and can be captured by a two-parameter stochastic model.

The hippocampus is involved in encoding long-term memories of items and events from daily life in humans (1) and spatial environments in rodents (2). Each item (3), experience (4), or environment (5–7) is represented by a subset of active neurons among an often much larger number of inactive neurons. For spatial representations, the active subset consists of place cells, each of which fires when the animal is at specific locations in an environment (called the place fields of that cell) (8). The inactive neurons, which fire few or no spikes throughout the environment, are called silent cells (5). When an animal encounters another environment, a different subset of neurons becomes active, and this difference is believed to be the basis by which spatial contexts are distinguished (7, 9). Within a given environment, the fields of different cells together cover the space and are thought to provide a cognitive map enabling flexible navigation (2).

In environments typically used to study spatial firing (<5 m total track length or <1 m² for open arenas), ~20-50% of pyramidal neurons from the dorsal CA1 subregion of the rat hippocampus are recruited to be place cells (5, 6, 10), and most have a single place field. Wild rats have home ranges typically up to 50 m across, sometimes extending to hundreds of meters (11), and in larger laboratory environments (up to 18 m long or 3 m²) more neurons are recruited to be place cells, many cells have multiple fields, and place fields are wider (12-14).

However, far less is understood about the organizing principles of hippocampal spatial maps. Basic questions remain with implications for the underlying mechanisms and proposed functions of hippocampal representations. When fields are formed, which cells do they come from? Place fields are the units of spatial representation in CA1 and their distribution among cells determines how they code for location. Will every cell

become a place cell if the environment is large enough? If all cells became place cells, the specificity of their active subsets would disappear, requiring other mechanisms for retrieving the appropriate context from memory.

We therefore employed the largest maze to date and quantified two key aspects of the hippocampal map — which cells fire and where they fire — as it was being established. We recorded 253 putative pyramidal cells from dorsal CA1 (fig. S1) in 5 rats as they explored a 48-meter-long track (fig. S2). The track and room were both entirely novel to the animal. To test if there was a limit to recruitment, we challenged the representational capacities of the hippocampus by progressively extending the track in stages and making locations along the track as distinct as possible. In each epoch the animal traversed the current total length of track 3-5 times, and between epochs was confined to the original start location while the track was extended. Total track lengths in the four epochs were 3, 10, 22, and 48 m. Although animals traversed the entire available track during each epoch, to focus on the initial recruitment of cells and fields we restricted analysis to periods when the animal explored the additional novel sections of track introduced in each epoch. We only analyzed neurons that could be isolated in sleep periods flanking behavioral periods to ensure accurate counts of silent cells (5, 6).

In each new section of track, existing place cells formed additional fields and new place cells were recruited from the pool of silent cells (12) (Fig. 1 and figs. S3-S5). The multiple fields of individual cells appeared to be irregularly spaced over the track (Fig. 2A). The simplest model of place field formation is that the location of the fields of each cell follows a spatial Poisson process; that is, the locations are random and described only by a certain average rate. For cells with ≥ 6 fields (61/253), neither the spatial

distributions of fields nor inter-field interval distributions differed from the Poisson model (Anderson-Darling test, 0/61 cells, $p_{\text{FDR-adjusted}} < 0.05$) where they are uniform and exponential, respectively (Fig. 2, see fig. S6 for cells with < 6 fields).

We asked if a correspondingly simple model could describe the population as a whole (Fig. 3A). Specifically, did each cell have the same Poisson rate of field formation? This model would capture the qualitative behavior observed as environments increase in size — additional fields are formed and previously silent cells are recruited to be place cells. Quantitatively, this model makes certain predictions. First, the observed number of fields per cell would follow a Poisson distribution. Second, the distribution of the location of each cell's field that is closest to the start of the track (called the recruitment curve, since it shows the fraction of the population that is recruited to be place cells as the track lengthens) would follow an exponential distribution. However, the fits of both distributions to the data were poor (Fig. 3, B and C), indicating that such a model does not describe hippocampal population representations in novel environments.

Instead, the observed number of fields per cell was overdispersed relative to the equal-rate-Poisson model (Fig. 3B and fig. S7A), indicating significant differences in the spatial rate of field formation between cells. That is, a few neurons had many fields while many more than expected had few or no fields. The recruitment of neurons into the representation reached only $\sim 65\%$ at 48 m (range 46-77%, fig. S7B), greatly undershooting the equal-rate-Poisson prediction. To see whether the $\sim 35\%$ of cells that remained silent were capable of forming fields at all, we later exposed the animal to a second novel environment and found that some of these cells formed clear place fields (fig. S8).

We next asked if the differing propensity of cells to form fields across the population could be described by a particular distribution. The number of fields per cell was well-fitted with a negative binomial distribution (Fig. 3B, parameters $r, p = 0.57, 0.14$), which can arise if each cell is an independent Poisson process with its rate drawn from a gamma distribution (fig. S9). Moreover, the recruitment curve under such a gamma-Poisson model would follow a Lomax / Pareto type II (power law) distribution. The predicted recruitment curve matched the observed one well (Fig. 3C, Kolmogorov-Smirnov statistic = 0.05, $p = 0.48$). The curve shows logarithmic-like recruitment over spatial scales spanning several orders of magnitude, including the range of distances traveled by wild rats (*11*), and its extrapolation predicts 90% recruitment at ~ 500 m.

We examined additional properties of the distribution of fields. As expected from independent Poisson processes, overall field density was uniform over the environment (Fig. 3D, K.S. statistic = 0.03, $p = 0.36$) and was uninfluenced by local track features or running speed (fig. S10), field propensities were stationary across the track (fig. S11), and field locations were uncorrelated between pairs of cells (fig. S12).

Memorylessness — being invariant to the starting point or history — is a defining property of Poisson processes. We thus chose evenly spaced points on the track, ignored whether or not cells had been recruited before that point, then determined the subsequent recruitment curve for the remainder of the track. These memoryless recruitment curves had the same shape regardless of the starting point (Fig. 3E and fig. S13).

The uniform field density at the single-cell and population level, exponential inter-field spacing, good match to the predicted recruitment curve, stable propensity distribution, uncorrelated field locations across cells, memorylessness of recruitment, and

uncorrelated spatial and non-spatial field properties (fig. S14) demonstrate that the gamma-Poisson model is a good statistical description of place field formation in a novel environment. Different criteria for place field detection did not change the results (fig. S15). While the gamma-Poisson model was sufficient to explain the recruitment of cells and fields under our experimental conditions, other studies have shown increased field density around goals (15) and changing recruitment over time (10, 16), indicating other factors can modulate field propensity.

Our attempt to challenge the representational capacity of the hippocampus revealed neither a hard limit to recruitment nor completely random recruitment. Instead, a skewed distribution of field propensities across the population led to logarithmic-like recruitment over a wide range of ethologically relevant distances. What causes place cells to fire has been the subject of intense investigation for decades; this finding adds another dimension to that question, namely, what causes a cell to have a particular rate of expressing place fields?

Two distinct mechanisms can give rise to the observed gamma-Poisson process (17), preexisting differences between cells (18) or a cumulative advantage mechanism during exploration (e.g. Polya-Eggenberger Urn). Firing rates in slow-wave sleep (SWS) before the animal had experienced the maze were moderately correlated with the subsequent number of fields per cell (Fig. 4A, $r = 0.45$, $p < 1 \times 10^{-13}$), providing evidence preexisting differences contribute to field propensities without, however, ruling out possible additional cumulative advantage mechanisms.

Preexisting differences between cells could result from differences in cellular excitability or network inputs. Future place cells are more excitable than future silent

cells before exploration (19), and artificially increasing the excitability of silent cells can convert them to place cells (20), linking preexisting intrinsic differences (21) with field propensity. Fixed cellular or network differences likely underlie the moderate variation in field propensity (22, 23) (fig. S16) with anatomical location.

Place fields are ultimately derived from spatial information originating from external sensory or self-motion sources. Preexisting differences, whether cellular or network-based, could act as an additional element in existing models of place field origin (24–26) by modifying responses to spatial inputs (20). The gamma distribution of field propensities we observed provides a specific constraint on mechanisms and models of place cell firing. The link between preexisting differences and field propensity could also account for preplay of novel environments (27) and correlated firing rates (28) and field propensities (fig. S17) across multiple environments.

What functions might a range of field propensities serve? Equal rates of random field formation would maximize the network's ability to uniquely encode distinct places. But with the observed gamma-distributed propensities, the proportion of cells with single fields would remain at ~5-10% over a wide range of environment sizes, potentially enabling a simple readout of location (Fig. 4B). Furthermore, equal propensities would make distinguishing environments based on their active subsets challenging because large-enough environments would recruit all cells. Instead, the observed distribution of propensities allows environments with a wider range of sizes to be distinguished based on their active subsets, even assuming each cell's propensity was permanently fixed (Fig. 4C and fig. S18). These features may also operate alongside the dorsoventrally-modulated range of CA3 field sizes (14) to efficiently encode differently sized environments.

Log-like recruitment has been seen in motor (29) and sensory (30) systems, suggesting that it may be a general feature of neural population coding, along with other functions of skewed distributions (28). In the hippocampus it could underlie a Weber-like perception of space. The quantitative description of spatial representations provides new insight into how the hippocampus may handle capacity for multiple items as well as single, extended experiences, and may have implications for representations and memory formation (31) in other systems.

References and Notes

1. W. B. Scoville, B. Milner, *J. Neurol. Neurosurg. Psychiatr.* **20**, 11–21 (1957).
2. J. O’Keefe, L. Nadel, *The Hippocampus as a Cognitive Map* (Oxford Univ. Press, Oxford, 1978).
3. R. Q. Quiroga, L. Reddy, G. Kreiman, C. Koch, I. Fried, *Nature*. **435**, 1102–7 (2005).
4. H. Gelbard-Sagiv, R. Mukamel, M. Harel, R. Malach, I. Fried, *Science*. **322**, 96–101 (2008).
5. L. T. Thompson, P. J. Best, *J. Neurosci.* **9**, 2382–2390 (1989).
6. M. A. Wilson, B. L. McNaughton, *Science*. **261**, 1055–1058 (1993).
7. S. Leutgeb, J. K. Leutgeb, A. Treves, M.-B. Moser, E. I. Moser, *Science*. **305**, 1295–1298 (2004).
8. J. O’Keefe, J. Dostrovsky, *Brain Res.* **34**, 171–175 (1971).
9. X. Liu *et al.*, *Nature*. **484**, 381–385 (2012).
10. M. P. Karlsson, L. M. Frank, *J. Neurosci.* **28**, 14271–14281 (2008).

11. D. E. Davis, J. T. Emlen, A. W. Stokes, *J. Mammal.* **29**, 207–225 (1948).
12. A. A. Fenton *et al.*, *J. Neurosci.* **28**, 11250–11262 (2008).
13. T. J. Davidson, F. Kloosterman, M. A. Wilson, *Neuron.* **63**, 497–507 (2009).
14. K. B. Kjelstrup *et al.*, *Science.* **321**, 140–143 (2008).
15. S. A. Hollup, S. Molden, J. G. Donnett, M. B. Moser, E. I. Moser, *J. Neurosci.* **21**, 1635–1644 (2001).
16. Y. Ziv *et al.*, *Nat. Neurosci.* **16**, 264–266 (2013).
17. O. Lundberg, *On Random Processes and Their Application to Sickness and Accident Statistics* (Almqvist & Wiksells, Uppsala, 1940).
18. M. Greenwood, G. U. Yule, *Journal of the Royal Statistical Society.* **83**, 255 (1920).
19. J. Epsztein, M. Brecht, A. K. Lee, *Neuron.* **70**, 109–120 (2011).
20. D. Lee, B.-J. Lin, A. K. Lee, *Science.* **337**, 849–853 (2012).
21. T. Jarsky, R. Mady, B. Kennedy, N. Spruston, *J. Comp. Neurol.* **506**, 535–547 (2008).
22. E. J. Henriksen *et al.*, *Neuron.* **68**, 127–137 (2010).
23. K. Mizuseki, K. Diba, E. Pastalkova, G. Buzsáki, *Nat. Neurosci.* **14**, 1174–1181 (2011).
24. M. Tsodyks, T. Sejnowski, *Int. J. Neural. Syst.* **6**, 81–86 (1995).
25. T. Hartley, N. Burgess, C. Lever, F. Cacucci, J. O’Keefe, *Hippocampus.* **10**, 369–379 (2000).
26. T. Solstad, E. I. Moser, G. T. Einevoll, *Hippocampus.* **16**, 1026–1031 (2006).
27. G. Dragoi, S. Tonegawa, *Nature.* **469**, 397–401 (2011).

28. G. Buzsáki, K. Mizuseki, *Nat. Rev. Neurosci.* **15**, 264–278 (2014).
29. H. S. Milner-Brown, R. B. Stein, R. Yemm, *J Physiol.* **230**, 359–370 (1973).
30. M. A. Muniak, S. Ray, S. S. Hsiao, J. F. Dammann, S. J. Bensmaia, *J. Neurosci.* **27**, 11687–11699 (2007).
31. A. J. Silva, Y. Zhou, T. Rogerson, J. Shobe, J. Balaji, *Science.* **326**, 391–395 (2009).

Acknowledgments

We would like to thank M. Karlsson, J. Osborne, and M. Copeland for technical assistance and S. Druckmann, J. Dudman, A. Hantman, J. Cohen, and D. Lee for valuable comments on the manuscript. This work was supported by the Howard Hughes Medical Institute.

Figures

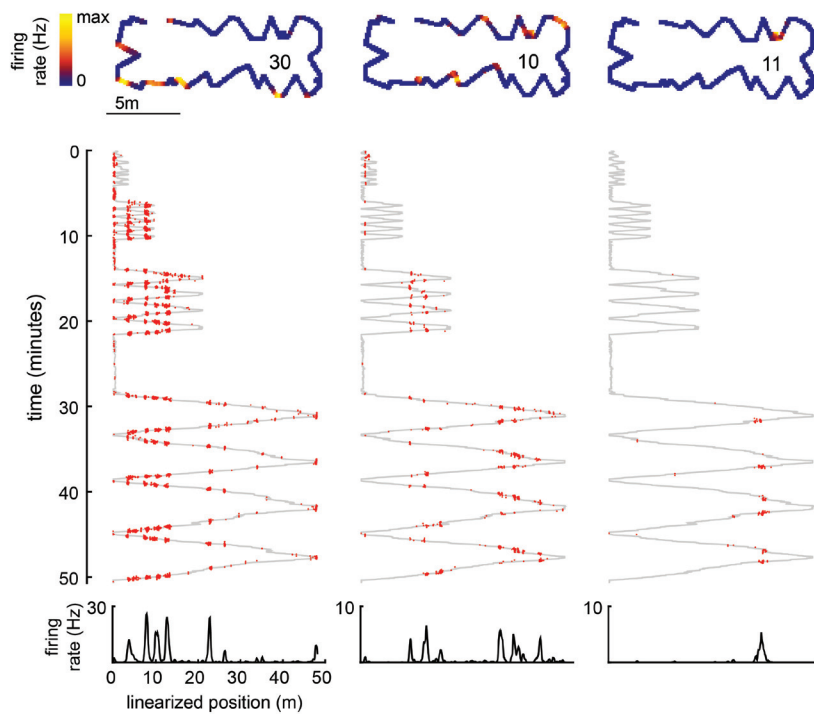


Fig. 1. Place cells form multiple peaks in large environments. For three neurons: firing rate on 48-meter-long track with peak rate noted (top), linearized position of animal (gray) and spikes (red) (middle), linearized firing rate (bottom). Spikes when animal speed < 5 cm/s excluded.

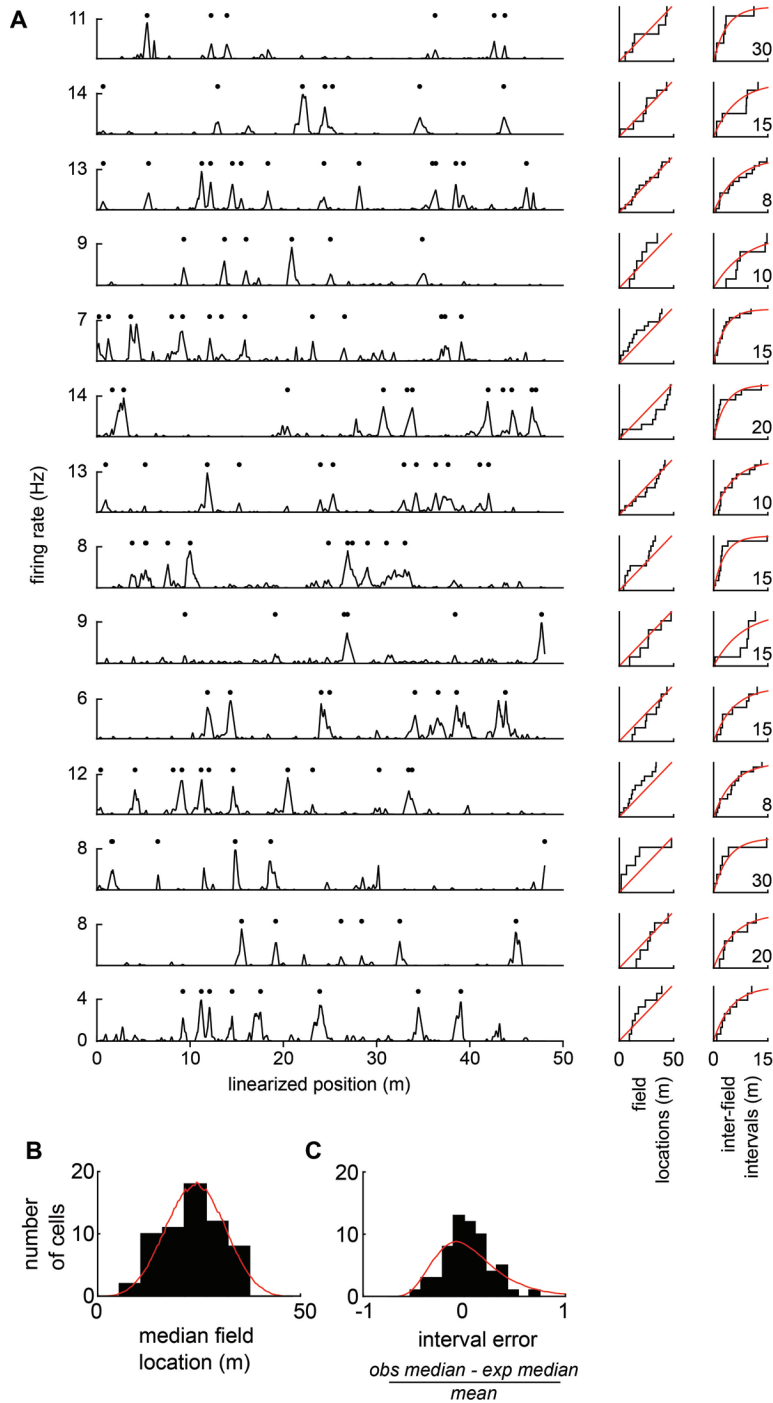


Fig. 2. Place field formation in individual cells is well-described as a spatial Poisson process. **(A)** All cells with ≥ 6 place fields from a single animal showing centers of detected fields (above). Cumulative distributions of field locations and inter-field

intervals shown to side (black), with the uniform and exponential distributions expected for a Poisson process (red). **(B)** Distribution of median field location (black) of all cells with ≥ 6 fields across animals ($n = 61$ cells from 5 rats) versus distribution expected for cells with uniformly distributed fields (red). **(C)** Distribution of deviation from exponential of median inter-field interval (normalized by the mean interval) for all cells with ≥ 6 fields. Distribution expected for cells with exponentially distributed fields (red).

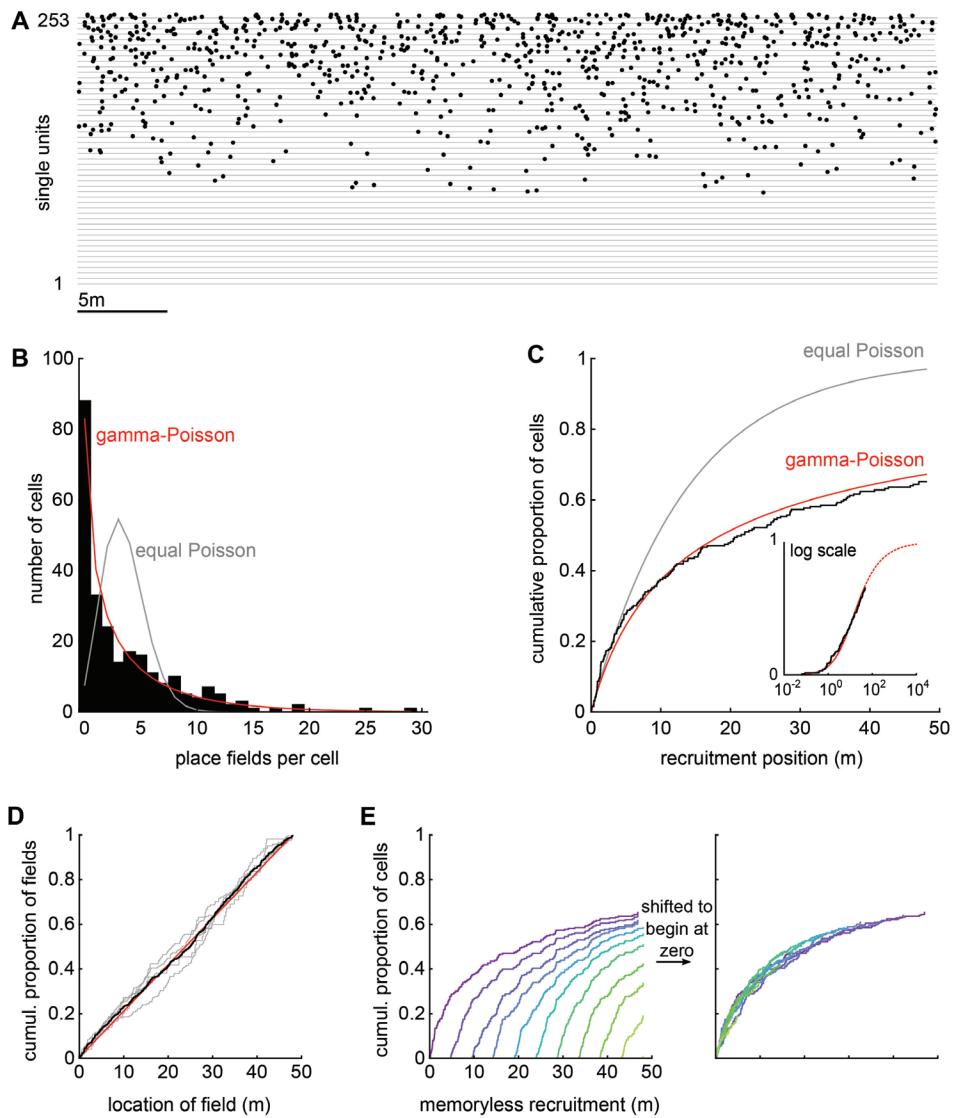


Fig. 3. Statistical, population-level model of the formation of hippocampal spatial representations. (A) Place field locations of all 253 recorded neurons. Lines show extent of the track every 5 cells. Cells sorted by number of fields. (B) Number of place fields per cell. Distribution assuming each cell has equal Poisson rate (given by the mean number of fields per cell) of forming place fields per unit length (gray). Fit of negative binomial distribution (red), which results from gamma-distributed Poisson rates (i.e. gamma-distributed field propensities). (C) Recruitment curve, derived from location of

field closest to start (0 m) for each cell, representing the proportion of place cells in the entire population as function of track size. Predictions of equal-rate-Poisson (gray) and gamma-Poisson (red) models, each using parameters estimated from (B). **(D)** Distribution of all fields across animals (black) along track versus constant-density uniform distribution (red). Individual animals (gray). **(E)** Memoryless recruitment curves constructed by starting at a point along track then calculating subsequent recruitment regardless of activity in previous length of track. Same curves shifted to allow comparison of shapes (right).

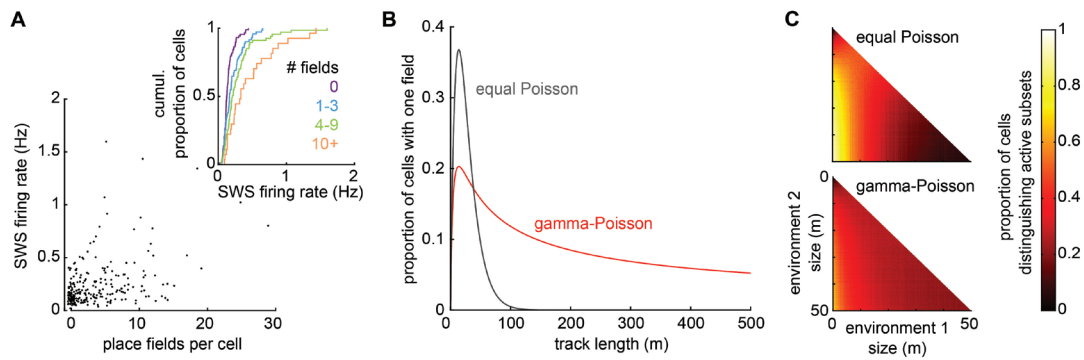


Fig. 4. Origin and coding implications of the distribution of field propensities. **(A)** Firing rates in slow-wave sleep (SWS) before exploration were correlated with subsequent number of fields per cell on track (jitter added for visualization). SWS firing rates separated into groups by number of fields (inset). **(B)** Proportion of cells with exactly one place field as a function of environment size under equal-rate-Poisson and gamma-distributed models of field propensities. **(C)** Simulation of the expected proportion of neurons that are place cells in one environment and silent in another for environments of different sizes under the two models.

Supplementary Materials for

Large Environments Reveal the Statistical Structure Governing Hippocampal Representations

P. Dylan Rich*, Hua-Peng Liaw, Albert K. Lee*

*To whom correspondence should be addressed. Email: richp@janelia.hhmi.org;
lea@janelia.hhmi.org

Materials and Methods

Subjects

The subjects were five adult male Long-Evans rats, 400-500 g at the time of surgery. Animals were individually housed in 30 × 35 × 40 cm cages after surgery on a 12-h light 12-h dark schedule. Testing was performed during the dark phase. Animals were food restricted at >85% of their free feeding weight. All procedures were performed according to the Janelia Farm Research Campus Institutional Animal Care and Use Committee guidelines on animal welfare.

Surgery, electrode targeting, and training

Rats were anesthetized with isoflurane and mounted in a stereotaxic frame. A craniotomy was performed over the CA1 field of the right dorsal hippocampus (AP -3.7 mm, ML 2.4 mm) and the dura removed. A microdrive holding 16 individually adjustable tetrodes and 4 individually adjustable reference electrodes was implanted over the site. Tetrode wire was nickel-chromium and 17/12.5 μ m in diameter with/without insulation. The tips of tetrodes were gold-plated to reduce the impedance of each channel to <250 k Ω at 1 kHz. A screw over the left cerebellum served as ground for recordings.

Following surgery electrodes were adjusted over a number of weeks to descend to the pyramidal cell layer of CA1, using electrophysiological features such as the amplitude and polarity of the sharp wave and the amplitude of units.

Animals were trained to run on linear tracks and open field mazes for Froot Loop rewards (crushed and mixed with water). No maze the animal explored as part of the training was especially large (<2m in maximal extent).

Experiment

To study the process of recruitment as it was happening, we performed the experiment in an entirely novel room which animals had not visited or seen before. The room was normally used during the work week for cage cleaning. For all but one animal, the room was partitioned with a curtain such that, excluding occlusions from the recording equipment in the middle of the room, animals could see the whole room (~150 m²) from any point of the track (fig. S2). For the animal without the curtain partition the L-shaped space was ~180 m².

A 48-meter-long elevated linear track was laid out around the room. The track was designed to make each part as distinct as possible for the animals so that, in combination with the prominent distal visual cues, there was little risk of confusion as to where they were. Track segments were of various lengths (0.4-1.6 m) and were painted a variety of plain colors using high contrast patterns and with different textured paints. The track was arranged with a variety of gentle turns, switchbacks, and chicanes. The track was 9 cm wide with 3 cm high walls and was elevated ~30 cm from the floor.

On the day of the experiment, animals were brought in a cage with an opaque cover to a room adjoining the main experimental room. They rested on a towel in a high-walled sleep box for ~2 h before exploration. During this time (PRE, fig. S2), behavioral activity was monitored as we recorded neural data. After a sufficient period of rest had been recorded, animals were carried directly to the start of the first section of track (RUN1).

The track was divided into 4 sections: 3, 7, 12, 26 m in length, which would be explored cumulatively in turn (the total length of track in each epoch was 3, 10, 22, and 48 m). All sections apart from the first were dismantled and stored at the edge of the room before the start of the experiment. Animals initially traversed the first section 3-5 times. They were then confined to a small area at the start of the track while the second section was added to the end of the first. Animals then made 3-5 traversals of the full extent of the track, which now consisted of both the familiar section 1 and the novel section 2. This process of adding the next section and then traversing the whole track was repeated for the 3rd and 4th sections of track in turn. Each novel section was longer than the last to attempt to maximally challenge the representational capacities of the hippocampus/animal.

Once the animals had explored the track, they were returned to the sleep box. After at least 4 h (at most ~5 h), they were returned to the long track where they ran an additional 4-5 laps (RUN2). Following this, the animals were immediately brought to an oval-shaped open field (~40 × 100 cm) maze in a separate room, which they explored for 10-25 minutes (RUN3). Another sleep session (POST) followed this exploration.

Either immediately following the experiment or within a few days of it, 3-4 tetrodes were electrolytically lesioned (20 μ A for 10 s) as fiducials and animals were transcardially perfused with phosphate-buffered saline followed by a 4% paraformaldehyde solution. Brains were cut in 50 μ m sections and stained with cresyl violet. Fiducial lesions, electrode tracks, and the relative locations of the tetrode guide cannulas in each microdrive, as well as allowance for brain shrinkage were used to estimate the AP and ML coordinates of each tetrode with respect to a rat brain atlas (32). Only tetrodes localized to the CA1 region were used in analysis (fig. S1). The atlas was used to construct a three-dimensional model of the CA1 pyramidal cell layer, allowing an estimate of the tetrode locations with respect to the septotemporal and proximodistal axes of CA1.

Neural data were recorded using a 64-channel system. In order to record neural activity from animals continuously through rest periods in the sleep box, exploration of the long track, and exploration of the open field maze, we devised a mobile cable counterweight system (MCCS, fig. S2). The MCCS consisted of a wheeled wooden upright (~2 m tall) and an extended wood armature (~1.5 m) from which a 5 m fine wire cable was suspended. The counterweight for the fine wire cable was concealed in a PVC tube attached to the upright and allowed animals to move around freely in a relatively large area near the MCCS. An experimenter followed each animal with the MCCS,

staying close enough such that there was enough slack for the animal. A 40 ft shielded cable connected the MCCS to the recording system. Spikes were detected by a 60-70 μ V negative threshold on a 600-6000 Hz filtered signal and waveforms (32 samples at 32 kHz) were captured around each threshold crossing. LFP (0.1-9000 Hz) was recorded continuously at 32 kHz.

Spike sorting

Spike sorting was performed in MatClust (33) using the peak amplitude of spikes on the four channels of each tetrode. Units were initially identified in the PRE sleep session and clustered there entirely blind to their activity in subsequent behavioral and sleep periods. Only units that could then be isolated and tracked over the entire experiment (PRE, RUN1, REST, RUN2, RUN3, POST) were included in the analysis. This was done to ensure accurate estimates of the silent cell fraction. Putative interneurons were excluded based on high firing rates during behavioral and sleep periods and narrow-width waveforms, with the remainder of units classified as putative pyramidal neurons. The L-ratio and isolation distance (34) were calculated using the peak amplitude data. There was no correlation between these cluster quality metrics and the number of fields determined for each unit (fig. S3). The number of isolated putative pyramidal units from tetrodes localized to CA1 from each animal was 63, 58, 24, 57, and 51.

Position tracking

The position of the animal was reconstructed from video taken by 3 wide angle overhead cameras. Video was synchronized to the timestamp clock from the acquisition system using a timestamp video titler. In whichever section of track the animal was in, the animal's position was manually traced in the corresponding video file; additionally each vertex of the track which appeared in each video was marked. The position of the animal on the track was then reconstructed by converting the points relative to each vertex from the video to a scale model of the track constructed from measurements and photographs taken when the track was assembled.

Place field determination

In order to isolate the initial recruitment of place cells and fields, only times when the animal was exploring a novel section of track (the entire first section of track in the first epoch or the newly extended section of track in subsequent epochs) were considered. We excluded both times when animals were confined to the very start of the track and when they were traversing an already explored section of track from a previous epoch. This ensured that fields from all parts of the track were derived from similar amounts of sampling and that continuing refinements to the representation in the more familiar sections of track were separated from our study of recruitment of novel place fields. We used a minimum number of laps to estimate novel place fields; once animals had

explored a novel section sufficiently (3-5 laps), we confined them at the start and added the next section.

For each of the two directions of movement along the track we constructed linearized rate maps by taking the number of spikes in each 1 cm spatial bin of the track divided by the occupancy in that bin. Both were smoothed with a Gaussian kernel with a standard deviation of 10 cm and bins were discarded if the occupancy was not greater than 0.001 s/cm. Only periods when the animal's velocity was greater than 5 cm/s were included in the spatial firing rate maps. Velocity was calculated as the net linear track displacement in a sliding 1 s window; the sign of the velocity gave the direction of travel along the track, either outbound (away from the start) or inbound (towards the start). Two-dimensional rate maps used for display were calculated in an analogous manner using a 2D Gaussian with standard deviation 10 cm for smoothing,

A place field was defined as at least 15 contiguous cm of the linearized rate map in which the firing rate exceeded 2 Hz. The field width was delimited by the points where the firing rate went below 2 Hz. Given the lower than usual sampling in the large environment, we also excluded fields that did not have at least 1 spike in at least 50% of passes through the field in the direction being considered. Since in linear tracks place fields may be directional (35), place fields were detected independently for each directional firing rate map, outbound and inbound, then fields in different directions were merged if either field showed at least 50% overlap with the other (fig. S4). The center of the field, the field location, was defined as the peak of the rate map within the field. For merged fields the peak was taken as the peak of the averaged directional rate maps. Cells without fields had very low firing rates (0.006 ± 0.01 Hz, mean \pm std) in the environment, lower than cells with at least one place field (fig. S5).

For the open field used during RUN3, position was tracked either manually as for the long maze, or automatically with an LED. Two-dimensional rate maps for each cell were constructed with a Gaussian with standard deviation 5 cm. Fields were detected as at least a 100 cm^2 contiguous region of 1 cm^2 bins where the firing rate exceeded 2 Hz.

Poisson testing

In testing whether the field formation for individual cells was well-described by a Poisson process, we examined the distribution of field locations and distribution of inter-field intervals. For cells with at least 6 place fields, we tested whether the field locations could be described by a uniform distribution and the inter-field intervals by an exponential distribution using the Anderson-Darling goodness of fit test. We used the Anderson-Darling test due to its sensitivity when using low numbers of samples. P-values were adjusted for each set of tests to control the false discovery rate (36). Inter-field intervals were calculated agnostic to the directionality, if any, of fields. In order to inspect the population for an overall bias in both location and intervals, we calculated two statistics for each cell: the location of the median field and the difference between the

observed and expected median inter-field interval under the exponential model. The inter-field interval error was normalized by the mean interval for each cell. Null distributions for the statistics were calculated by simulating 5000 uniform and exponential surrogate data sets for each cell with the estimated parameters under the model. For cells with fewer than 6 place fields, field distributions were not analyzed individually because of low field numbers. For these cells we pooled the locations of fields from cells with the same number of fields, and tested the compound process for uniformity using the Anderson-Darling test (fig. S6). We did not test the exponentiality of the compound processes because, though the data matches the exponential distribution well (fig. S6), it is not a stringent test of any underlying exponentiality of the individual cells.

Population models

The parameters of the equal-rate-Poisson and gamma-Poisson models were both estimated from the number of place fields from each cell using maximum likelihood estimation to fit the Poisson and negative binomial distributions, respectively. In the case of the equal-rate-Poisson model, this assigned to each cell a rate of forming fields equal to the observed mean number of fields per cell. The parameters of the models, estimated from the field number distributions, were then used to construct the predicted recruitment curves; the recruitment data itself were not used to fit these curves. The Kolmogorov–Smirnov test used to test the goodness of fit of the gamma-Poisson predicted Lomax recruitment curve was adapted to take into account the censored data (that is, some cells did not form place fields and so did not have a recruitment location). The K.S. statistic was calculated on the valid region of the cumulative distribution. To calculate significance, a Monte Carlo procedure was implemented (37). Two thousand surrogate samples with matched n were generated from the null distribution, censored using the range of the data (48 m) and the KS statistic was calculated for each. The distribution of null K.S. values was then compared to the real value to determine significance.

PRE slow-wave sleep correlation

We detected periods of slow-wave sleep (SWS) in the PRE session using a combination of behavioral and electrophysiological measures. Using an accelerometer mounted to the cable suspension pulley whilst the animal was resting in the sleep box, we were able to record when the animal was mobile. A 5 s buffer was added to either side of movement periods to give a robust estimate of immobile periods. Periods of putative rapid eye movement (REM) sleep were taken when the theta (6–10 Hz, 10th-order Butterworth) to delta (1–4 Hz 10th-order Butterworth) ratio, smoothed with a 2 s sliding window, exceeded a value of 2 for at least 0.5 s. Sharp wave ripples (SWRs) were detected as times when the amplitude between 150–250 Hz (8th-order Butterworth) exceeded a value of 3 standard deviations for at least 15 ms. SWS was defined as

immobile periods, excluding REM, that had a background rate of at least 0.2 SWRs per second.

Inter- and intramaze correlation comparison

Comparing the correlation of the field propensity for each cell within an environment with the correlation between two different environments is problematic if there is not equal sampling in the two cases. Since there were far fewer fields in the open field (because of its smaller size) compared to the long track, we used the following procedure (fig. S17). A random position along the long track was selected, then the number of fields per cell was counted moving forward along the track until the total number of fields matched the number of fields in the open field track, defining a window. Spearman's ρ correlation was calculated between the number of fields per cell inside the window and outside the window, giving an estimated within-environment correlation of field propensities. For the open field, the number of fields per cell in the open field was compared with the number of fields per cell outside the window in the long track, giving an estimated between-environment correlation. This was repeated 2000 times, to give a distribution of ρ for the two conditions, which gave the expected value (the median) and 95% confidence intervals.

Active subset simulation

For the simulation of the distinguishing active subset (Fig. 4C), we used the parameters of the gamma-Poisson and the equal-rate-Poisson models estimated from the data. For 300 independent environments ranging in size from 0.1 m to 50 m, we simulated the number of fields across a population of 1000 cells based on the fixed Poisson rate for each cell. The proportion of cells distinguishing active subsets was calculated for each pair of environments as the exclusive OR of whether a cell was active or not—that is, the proportion of cells that are in a different (active or inactive) state between environments. Additional conditions for the two environments were simulated (fig. S18). The proportion of cells with exactly one place field in environments of different sizes was calculated exactly from the gamma-Poisson model (fig. 4B).

Supplementary Text

Gamma-Poisson model and Lomax details

The gamma-Poisson model was originally developed by Greenwood and Yule (18). A modern description is given by Grandell (38). Briefly, a gamma-distributed variable Λ characterized by a shape parameter α and a rate parameter β

$$\Lambda \sim \text{gamma}(\alpha, \beta)$$

has a pdf which is

$$f_{\Lambda}(\lambda) = \frac{\beta^{\alpha}}{\Gamma(\alpha)} \lambda^{\alpha-1} e^{-\beta\lambda}$$

where Γ is the gamma function.

If X is a Poisson variable whose rate parameter is given by the gamma variable Λ

$$X \sim \text{poisson}(\Lambda)$$

then X is given by a negative binomial distribution (39),

$$\sim \text{negbin} \left(\alpha, \frac{\beta}{\beta+1} \right)$$

where

$$X \sim \text{negbin}(r, p)$$

$$P(X = x) = \frac{\Gamma(r+x)}{\Gamma(r)\Gamma(x+1)} p^r (p-1)^x$$

The waiting times, T , of a Poisson process with a rate λ are given by the exponential distribution

$$T \sim \text{exponentia } l(\lambda^{-1})$$

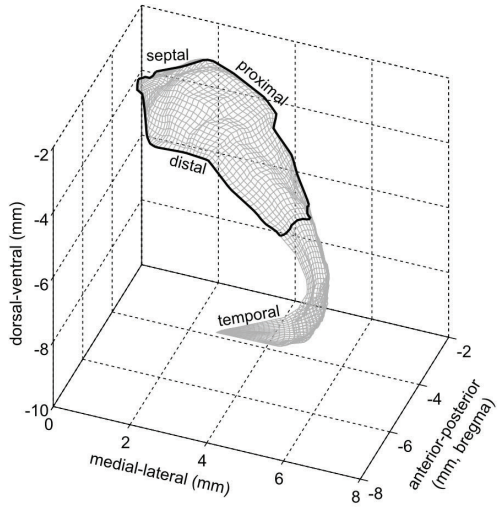
When the rate λ is a random variable, Λ , distributed as a gamma as above, the waiting times are a compound gamma-exponential distribution, which is a Lomax (Pareto type II) distribution (40) parameterized by the α and β from the initial gamma distribution

$$T \sim \text{lomax}(\alpha, \beta)$$

$$f_T(t) = \frac{\alpha\beta^{\alpha}}{(t+\beta)^{\alpha+1}}$$

Fig. S1

A



B

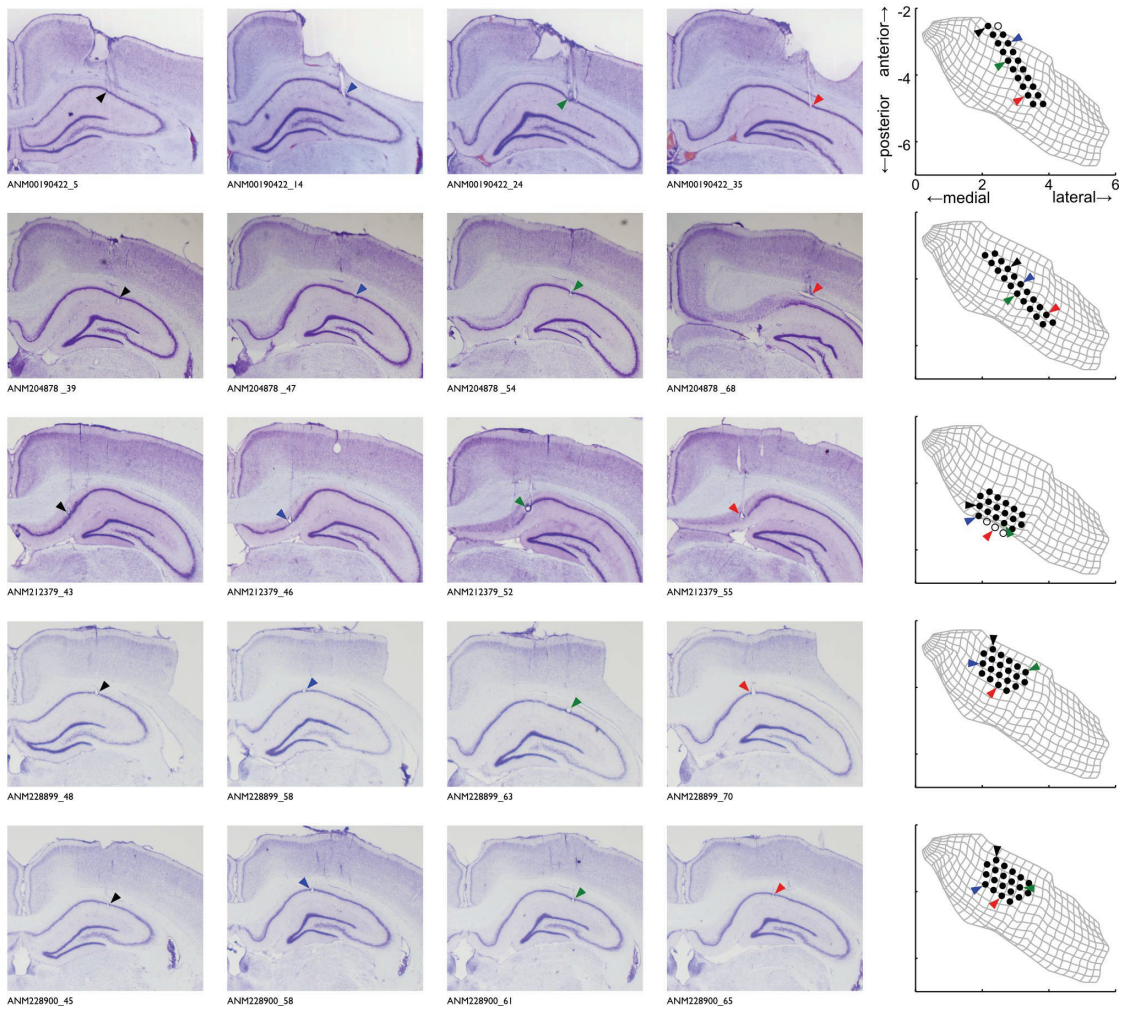


Fig. S1. Histological reconstruction of electrode locations. **(A)** A three-dimensional model of the CA1 pyramidal cell layer constructed using coronal sections from a rat brain atlas (32). The grid lines on the cell layer show the septotemporal and proximodistal axes of CA1. The septal half of CA1 is outlined in black and is displayed in top down views in **(B)**. **(B)** Individual histological sections (left) with the inferred position of each tetrode in CA1 (right). Colored arrows correspond to identified electrodes (based on electrode tracks for the animal in the first row, and electrolytic lesions for the other four animals). Unfilled circles show electrodes that were determined not to be in CA1.

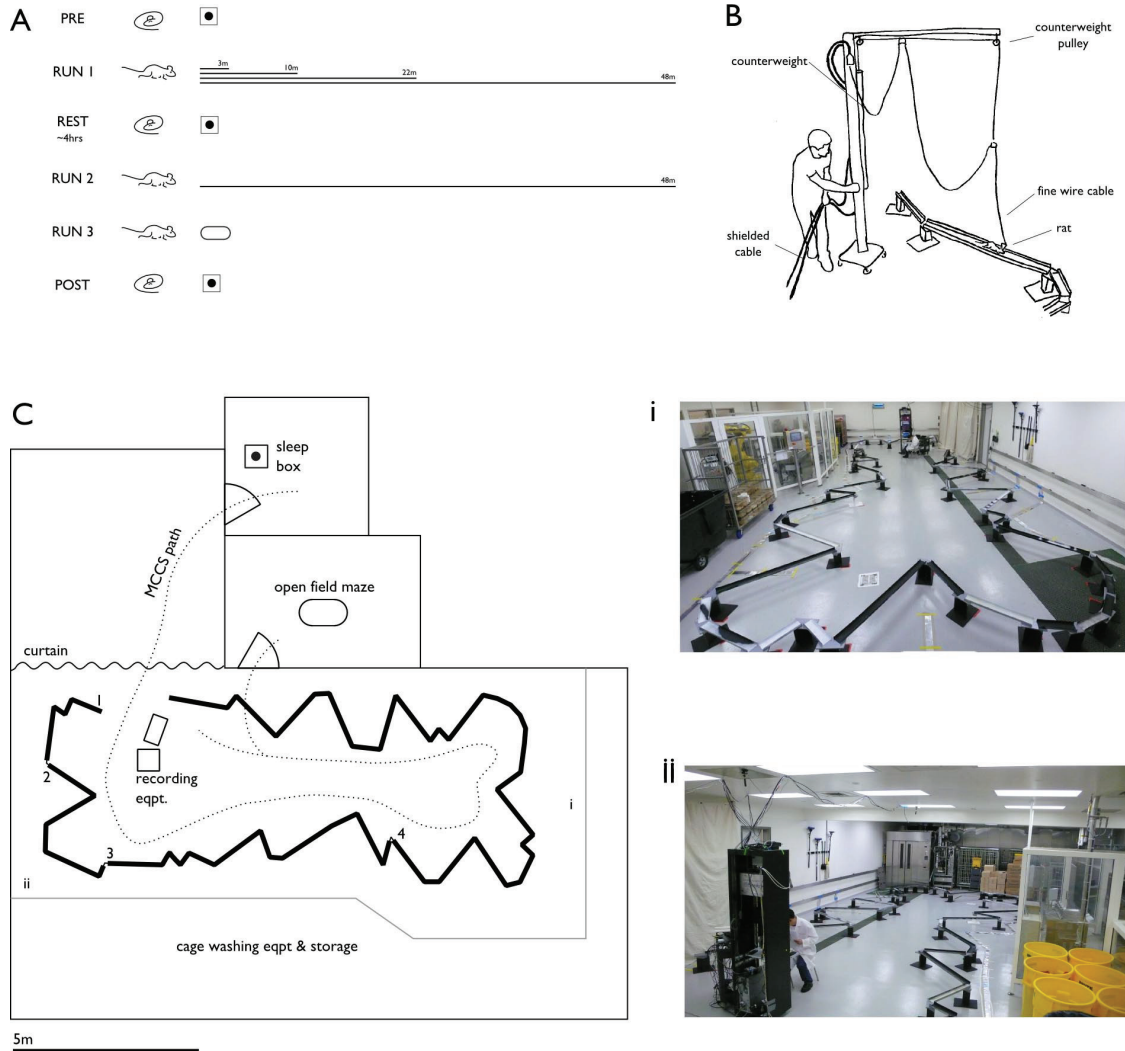


Fig. S2. (A) Experimental paradigm. (B) The mobile cable counterweight system (MCCS), operator, and animal running on the track. The MCCS allowed free movement of the animal along the track as well as in a separate sleep box and open field maze in separate rooms. (C) Scale drawing of the room in which experiments took place. The long maze was constructed in the large room, which for all but one animal was made rectangular with a floor to ceiling curtain. The sleep box and open field maze were in separate adjoining rooms to which the animal was carried while still connected to the MCCS. The start of the track section for each epoch of RUN1 is marked by numbers. The locations of two views of the room (i & ii) are also indicated.

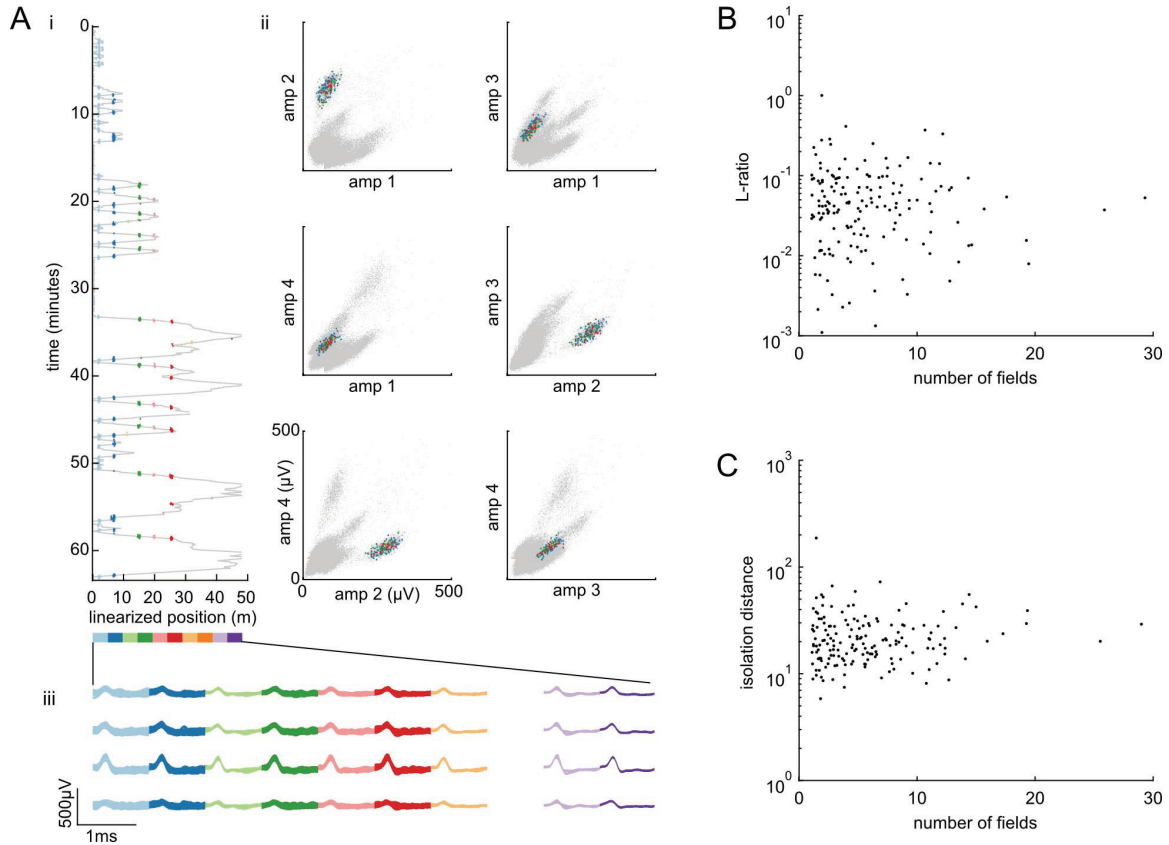


Fig. S3. Spike sorting and place fields. Multiple place field cells were not likely the result of clustering artifacts. **(A)** For a single unit we show the linearized position (i), tetra-peak amplitude projections (ii), and spike waveforms (iii). Spikes are color coded according to where on the track they were emitted, as marked by the color bar below the linearized position. The absence of bias in the waveforms and tetra-peak projections for each spatial bin indicates that the multiple fields were emitted by the same cell. Across the population, the number of fields from each unit was uncorrelated with the L-ratio **(B)**; Spearman's $\rho = -0.01$, $p = 0.86$) or the isolation distance **(C)**; Spearman's $\rho = 0.07$, $p = 0.37$) of each single unit cluster during RUN1.

Fig. S4 i

ANM00190422

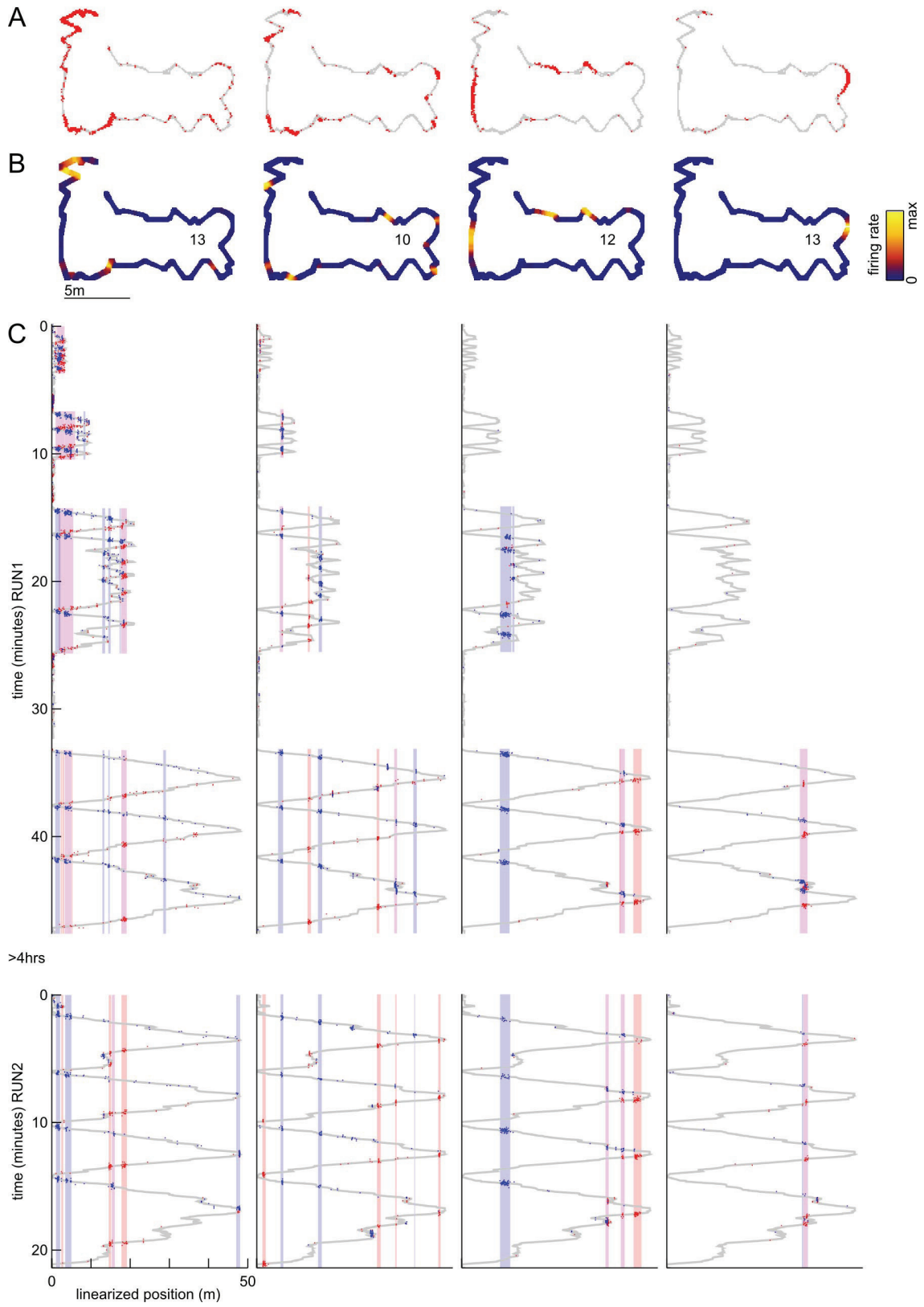


Fig. S4 ii

ANM204878

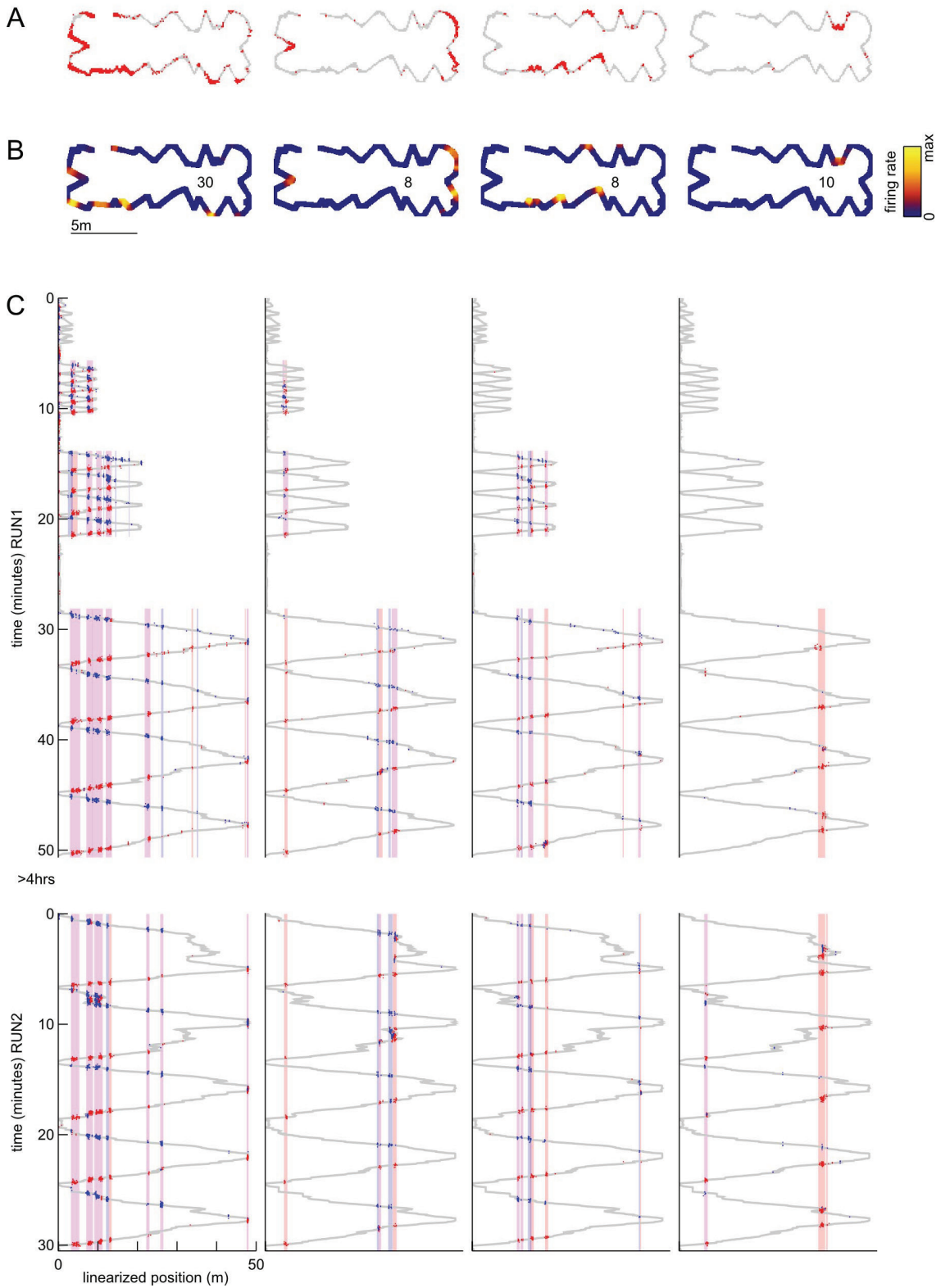


Fig. S4 iii

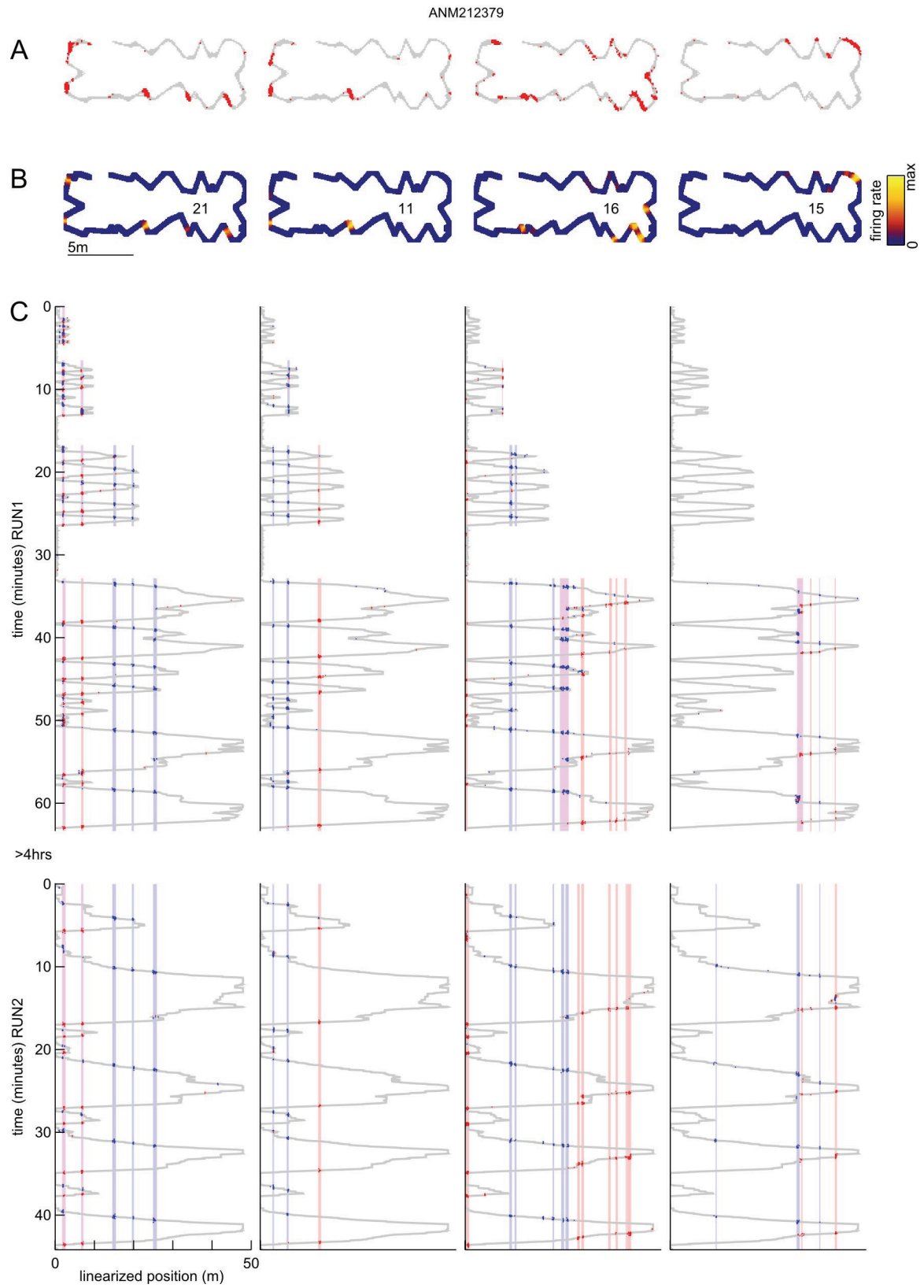


Fig. S4 iv

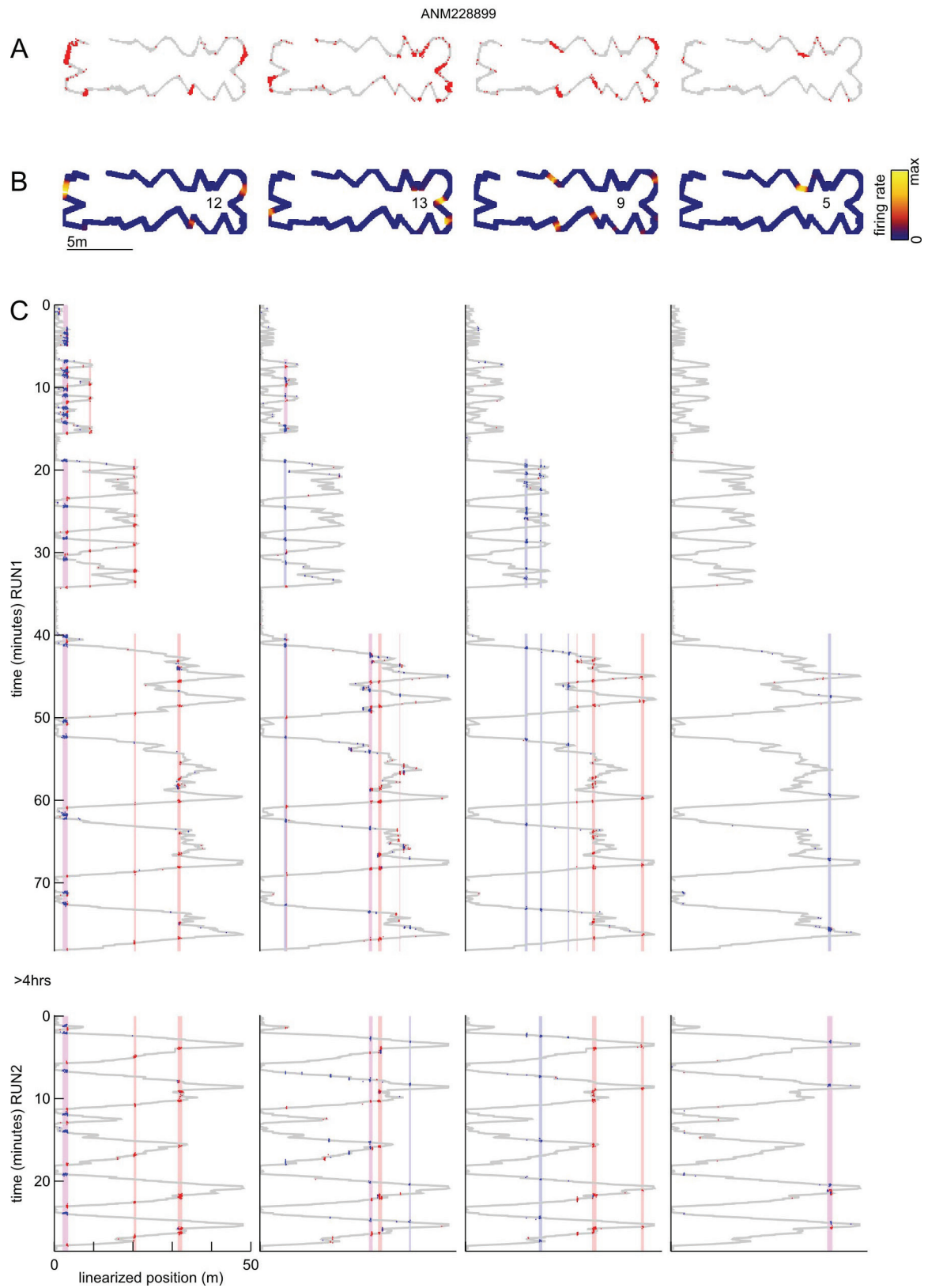


Fig. S4 v

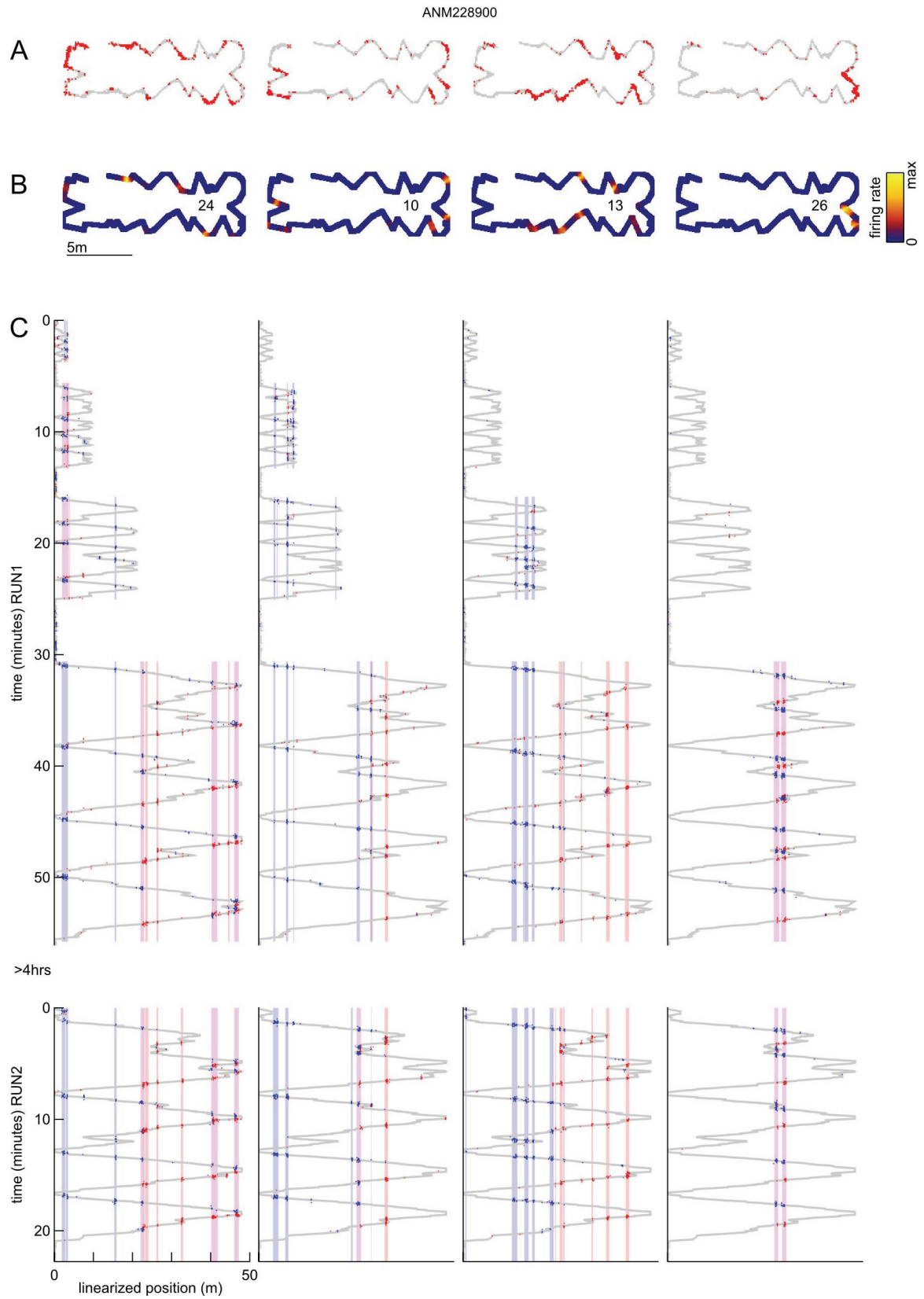


Fig. S4 i–v. Spatial firing of 4 individual cells from each of the five animals (i–v). Each column shows for each cell, **(A)** the position of the animal (gray) and the position of every spike (red), **(B)** the rate map calculated from the spatial firing (peak rate in Hz inset), and **(C)** the linearized position of the animal (gray) and spikes. For **(C)**, spikes in the outbound direction are in blue and inbound spikes are in red; horizontal jitter has been added to spikes to aid visualization. The spatial extent of detected place fields is shown as colored vertical bars for the corresponding direction. Place fields were detected independently for each of the four epochs of RUN1 and for the revisiting of the track at least 4 h later in RUN2, which is shown in lower part of the plot. For each animal we show a cell that was first recruited in the first, second, third, and fourth novel sections of the track in the corresponding epoch.

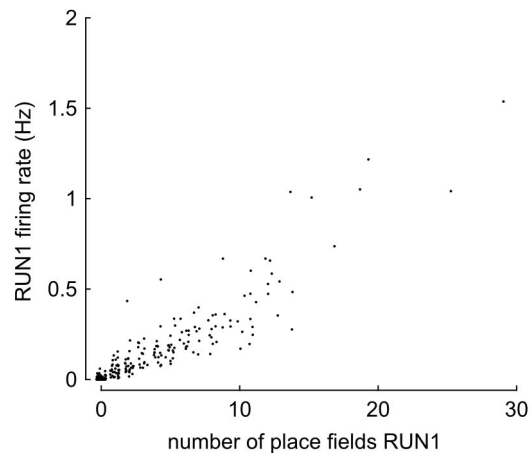


Fig. S5. The number of fields and the overall firing rate of each cell during exploration are tightly correlated. Run firing rate was calculated only considering periods when the animal was moving at $>5\text{cm/s}$. Horizontal jitter has been added to the number of place fields for visualization.

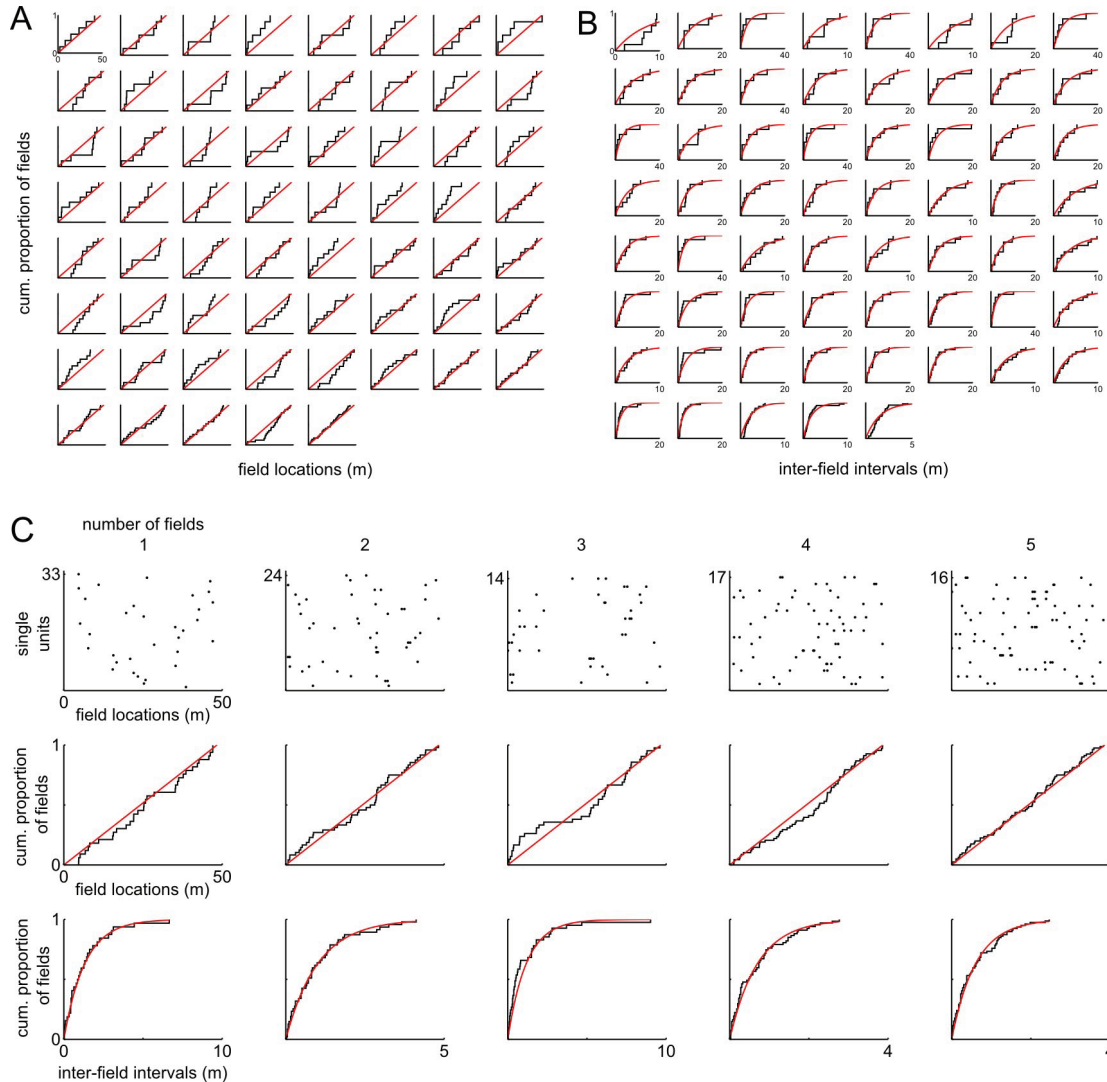


Fig. S6. Distribution of place field locations and of inter-field intervals for all cells. **(A)** The empirical cumulative distributions of field location for each cell with at least 6 fields, in black. In red is the expected distribution, uniform, under the Poisson model. **(B)** The empirical cumulative distributions of the inter-field intervals for each cell with at least 6 fields, in black. In red is the expected distribution, exponential, under the Poisson model. **(C)** Pooled data for cells with fewer than 6 fields. The top row shows the individual field locations for each cell, grouped by the number of fields. The middle row shows the pooled distribution of the locations, in black, and the expected distribution, uniform, in red. None of these distributions were significantly different from uniform (Anderson-Darling test, 0/5 $p_{FDR} < 0.05$). The bottom row shows the distribution of the inter-field intervals for the pooled data, in black, and the expected distribution, exponential, in red.

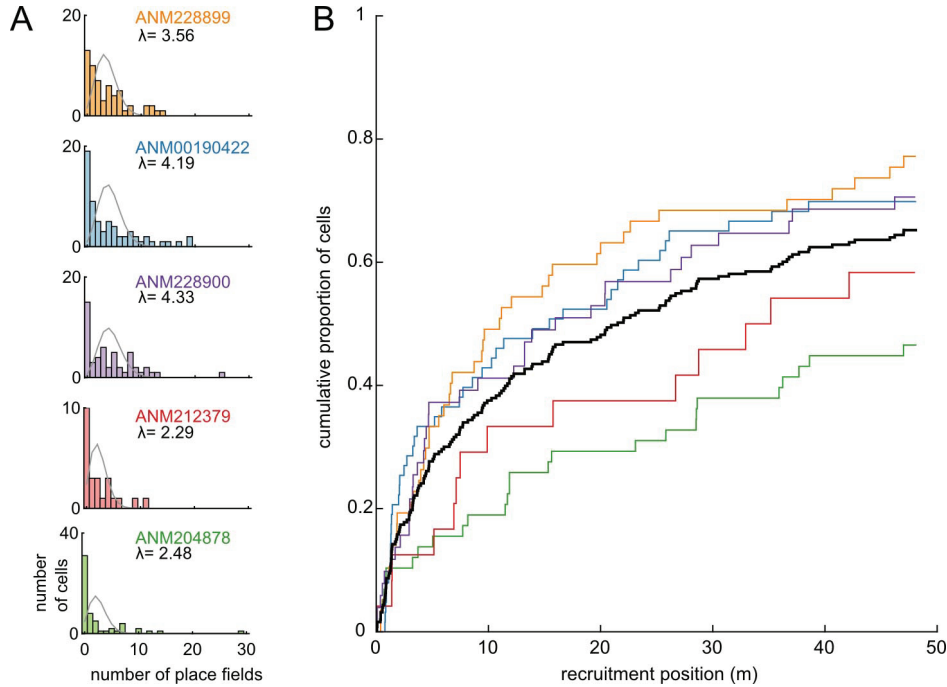


Fig. S7. Distribution of number of fields and recruitment curves for each animal. **(A)** Histograms of the number of fields of each cell for the five individual animals. The equal-rate-Poisson fit is shown in gray, using the average number of fields per cell (the rate parameter λ) from each animal. The fits for individual animals are poor, as is the case for the pooled data (Fig. 3B). **(B)** The corresponding recruitment curves for the five animals are shown in color. The recruitment curve pooled across animals (same as in Fig. 3C) is shown in black.

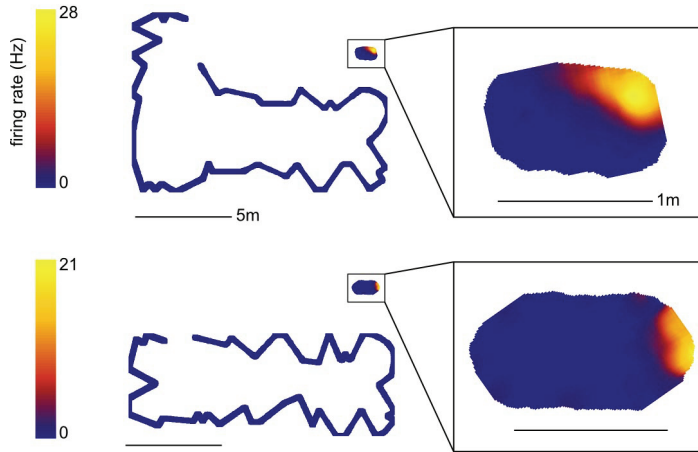


Fig. S8. Two cells which do not form place fields in the long-maze track (RUN1) that have place fields in the novel open field (RUN3). Rate maps are shown with the same color scale for each cell. The two environments are shown to scale. The insets show expanded views of the novel open field maze. The open field and long track were in different rooms.

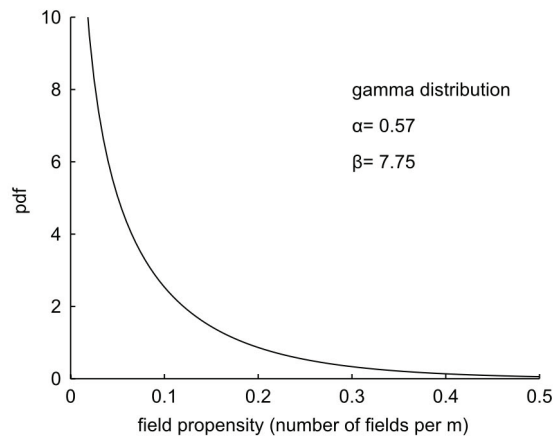


Fig. S9. Gamma distribution of field propensities. The probability density function of the distribution of inferred underlying field propensities across the population. Parameters were estimated from the observed distribution of the number of place fields per cell (Fig. 3B) under the gamma-Poisson model.

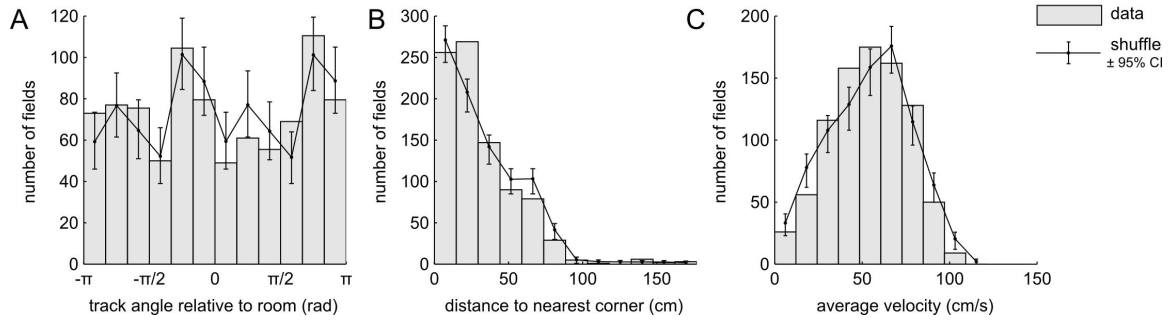


Fig. S10. No consistent trend of environmental and behavioral influences on field density. **(A)** The distribution of the number of fields as a function of the angle of the track with respect to the room. Nondirectional fields contributed half counts to their two directions. **(B)** The distribution of fields relative to the distance to the nearest track corner. **(C)** The distribution of the number of fields as a function of the animal's average velocity in 5 cm spatial bins along the track. Null models were made by shuffling the locations of the same number of fields as were counted randomly along the track and recalculating the distributions. The expected values for the shuffle and 95% confidence intervals were calculated from 2000 such simulations.

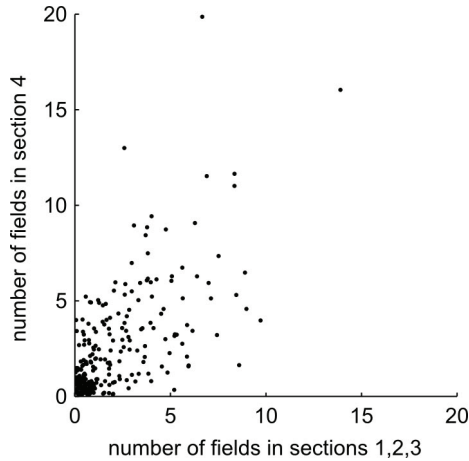


Fig. S11. Field propensities are preserved along the track. The correlation between the number of fields in the first three sections of track (which constitutes approximately the first half of the total length of the track) and the last section of track (which constitutes approximately the second half) did not significantly differ from that expected under the fitted gamma-Poisson model (Spearman's $\rho = 0.67$, $p = 0.95$, 2000 simulations using the parameters from the gamma-Poisson model). Each point represents an individual cell. Furthermore, there was no evidence of a change in propensities specifically at section boundaries as might be expected to occur if there was remapping when entering different sections. We computed the correlation of the number of fields per cell across sections (section 3 and an equally-sized piece at the start of section 4) and within a section (the same piece at the start of section 4 and a subsequent equally sized non-overlapping piece of section 4) and found no significant difference (Spearman's $\rho_{\text{across}} = 0.50$, $\rho_{\text{within}} = 0.38$; $p = 0.07$, p -value determined with 8000 shuffles of the number of fields in each piece). This was also the case for other sections (sections 2 and 3: $\rho_{\text{across}} = 0.32$, $\rho_{\text{within}} = 0.34$; $p = 0.84$; sections 1 and 2: $\rho_{\text{across}} = 0.28$, $\rho_{\text{within}} = 0.25$; $p = 0.78$).

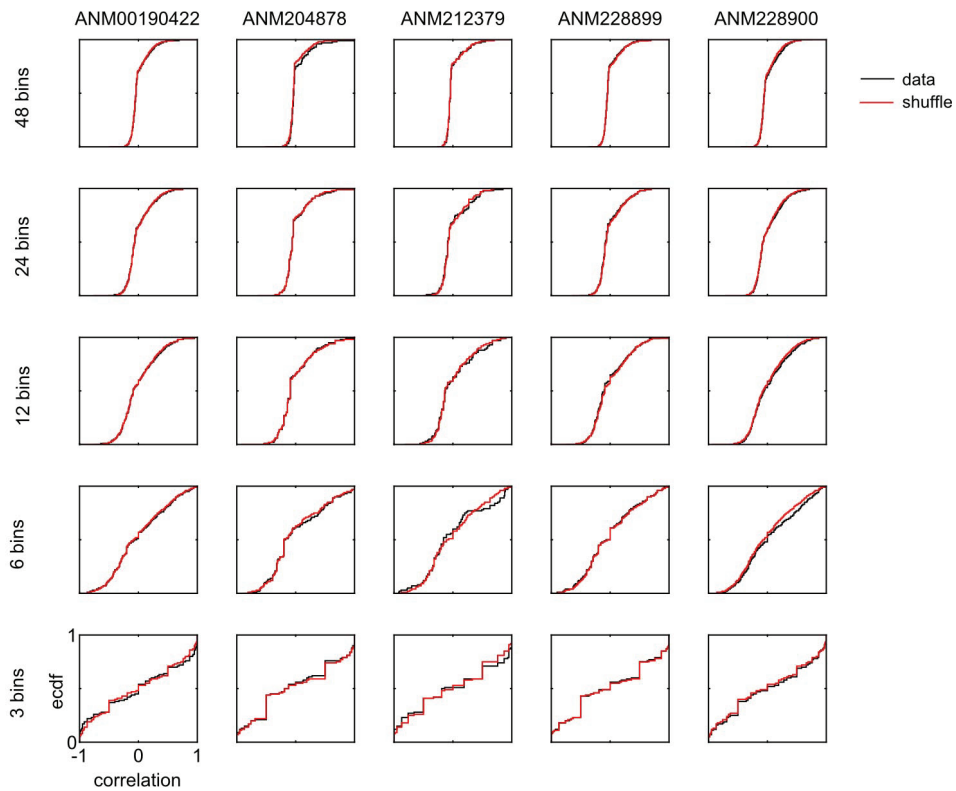


Fig. S12. The field locations of pairs of cells are uncorrelated. Each plot shows the distribution of correlations (Pearson's correlation coefficient) between the number of fields two cells have across spatial bins for every pair of cells from the same animal. The track was divided into either 48, 24, 12, 6 or 3 equal-sized spatial bins to test for various scales of correlation. In red is the distribution under the null model of independence between cells, calculated by shuffling the spatial bins for each cell 2000 times.

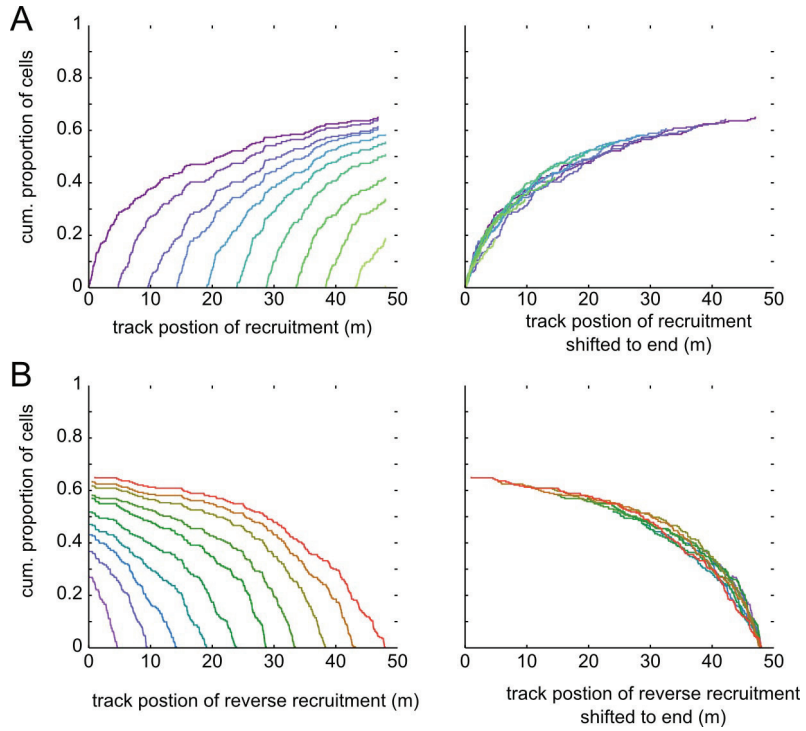


Fig. S13. Memoryless recruitment in the reverse direction. **(A)** Forward direction memoryless recruitment as shown in Fig. 3E. **(B)** Reverse memoryless recruitment curves were constructed by working backwards from the far end of the track. Curves show the same shape as each other as well as the forward direction memoryless recruitment curves.

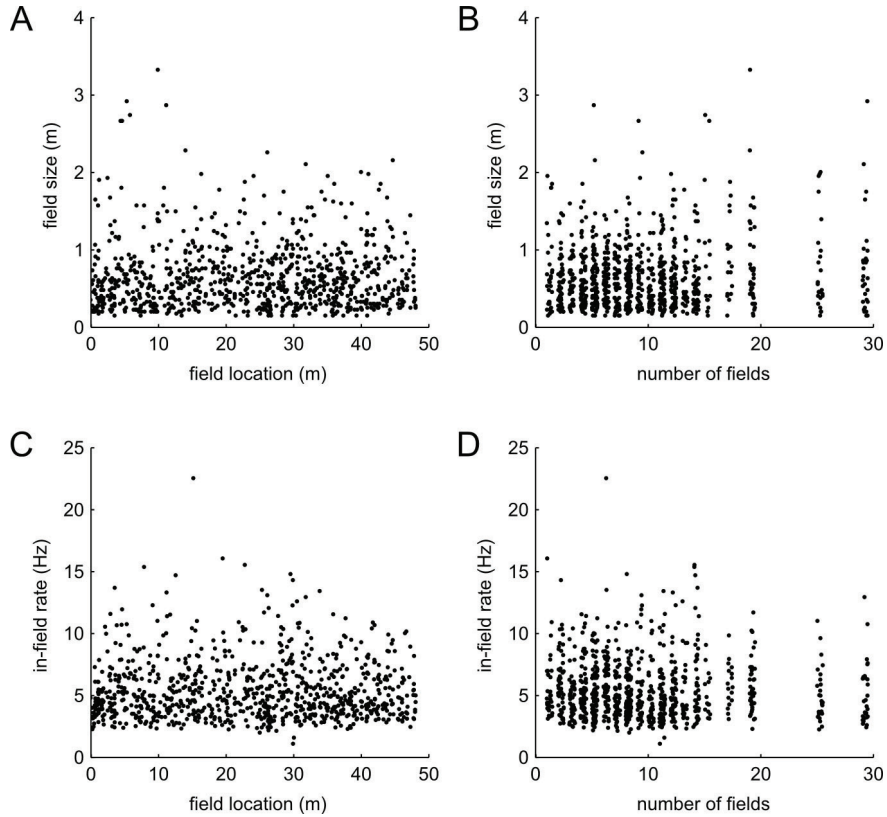


Fig. S14. Relationship between properties of individual fields imply that place fields are generic events emitted by the gamma-Poisson process. Basic parameters of individual fields, field size (65 ± 43 cm, mean \pm s.d.) and in-field rate (5 ± 2 Hz), were not correlated with location along the track (Spearman's $\rho=0.05, 0.01$, $p=0.11, 0.75$, **A** and **C**) or the number of other fields from the same cell ($\rho=0.05, 0.05$, $p=0.14, 0.17$, **B** and **D**). Jitter has been added to the number of fields in **B** and **D** to aid visualization.

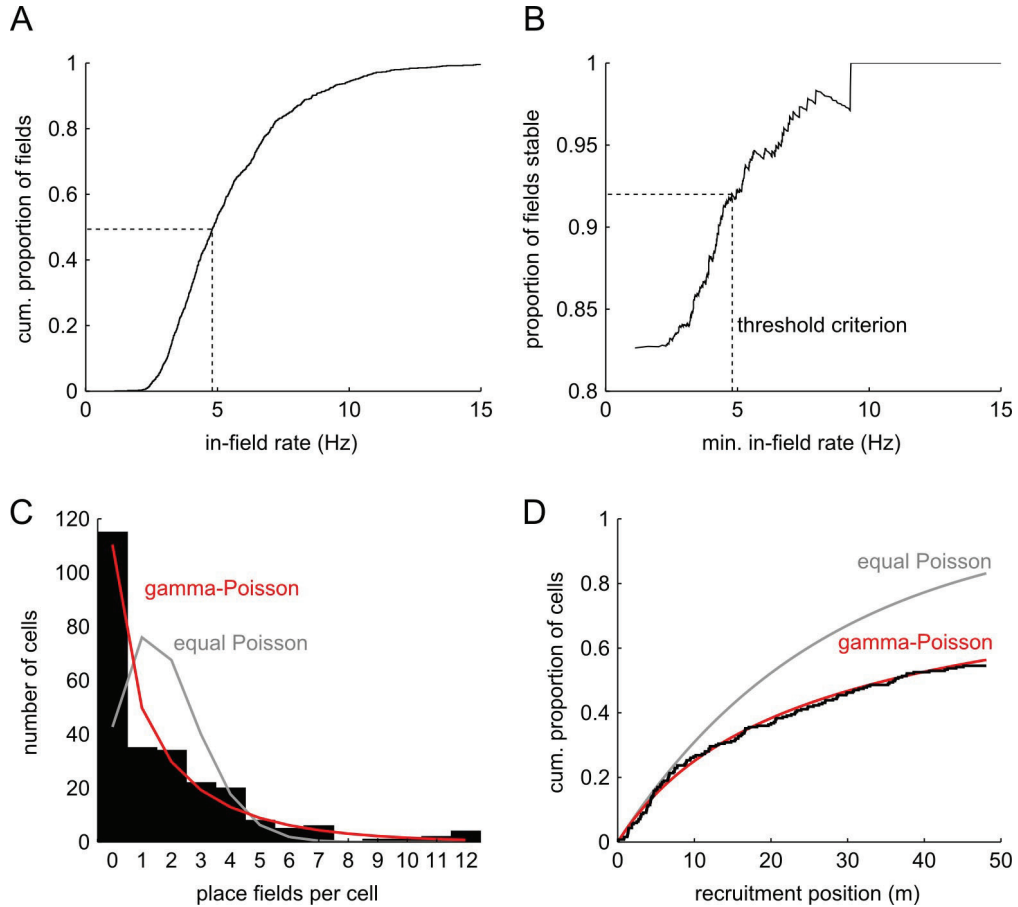


Fig. S15. The gamma-Poisson model remains a good fit to the data when using a higher threshold for place field detection. **(A)** The distribution of the field rate for all fields. Approximately 50% of fields had an average in-field firing rate of >4.8 Hz. **(B)** The relationship between minimum average in-field rate and the proportion of fields that were stable (as defined by firing in at least 50% of both the first half and the second half of passes through the field). The number of place fields per cell **(C)** and the recruitment of cells **(D)** was well-described with the gamma-Poisson model estimated in the same way as for all the fields (Fig. 3, B and C).

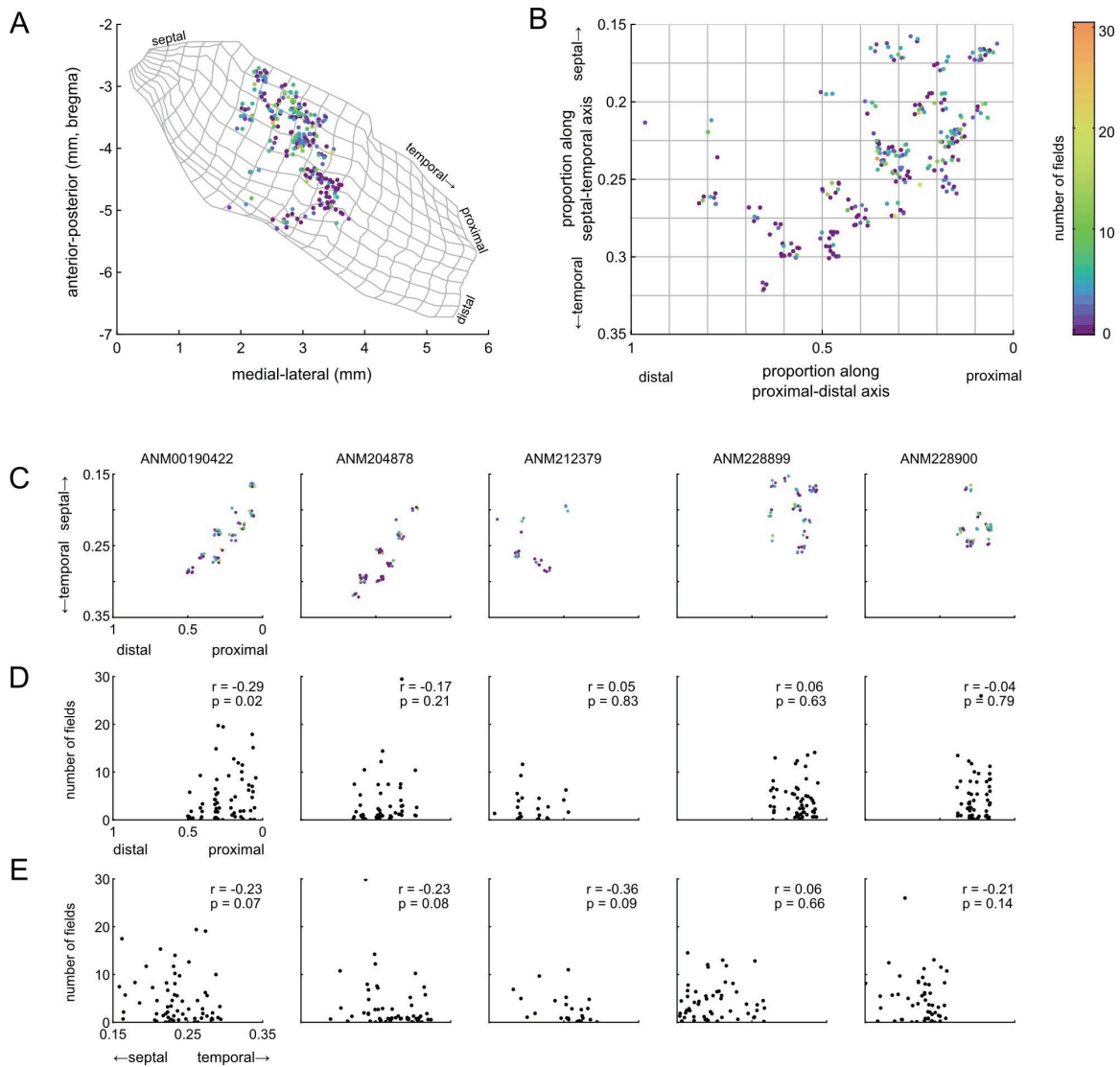


Fig. S16. Relationship of the number of fields for each cell as a function of anatomical recording location. **(A)** The location of each cell viewed from above the septal half of CA1 (as in fig. S1B), with the number of fields each cell has denoted by the color scale at the right. **(B)** The same cells as in **(A)** but plotted in terms of the relative septal-temporal and proximal-distal coordinates of CA1. **(C)** As in **(B)** but separated by animal. **(D)** and **(E)** show the number of fields per cell with respect to the two hippocampal axes, as well as the correlation coefficient and associated p-value. Although there was a weak relationship in the pooled data (ST $r = -0.20$ $p = 0.001$, PD $r = -0.19$ $p = 0.002$), this was not consistent within individual animals. Jitter has been added to all anatomical values and to the number of fields in **(D)** and **(E)** to improve visualization.

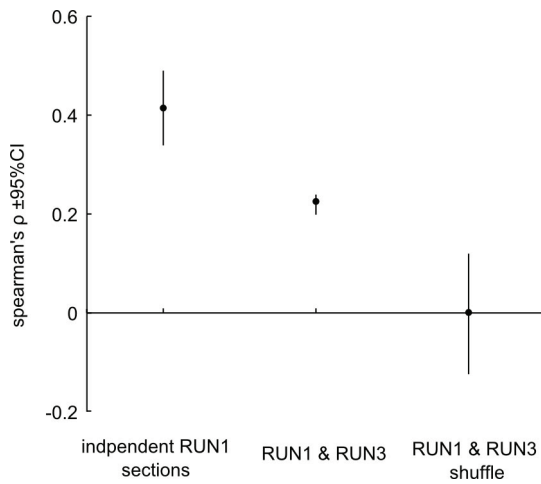


Fig. S17. Field propensities are correlated across environments but not as strongly as within a single environment. Correlation of the number of fields per cell between independent sections of long track (RUN1) and between the long track (RUN1) and open field arena (RUN3). The shuffle shows the expected variation under the null hypothesis of no correlation between environments. Note that the lower correlation value for the independent RUN1 sections compared to that between the two halves of the track (fig. S11) is due to attenuation of the estimated correlation as a result of using a smaller section of track for one of the independent RUN1 sections.

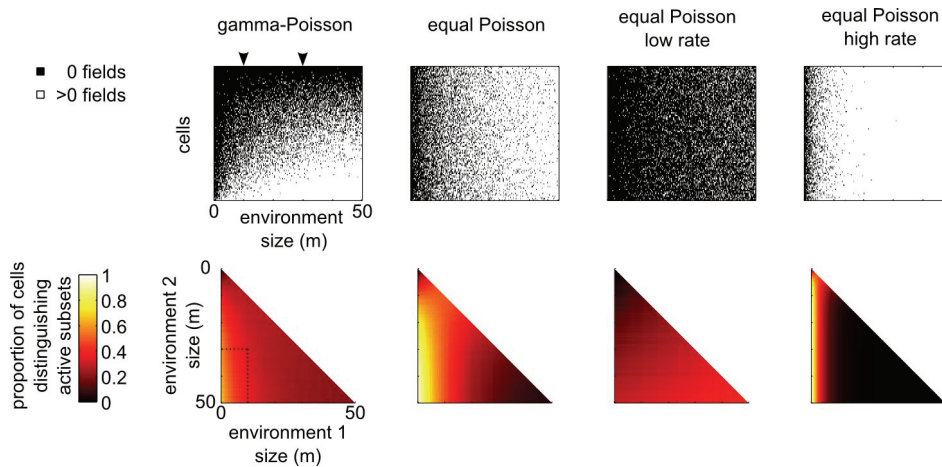


Fig. S18. Proportion of cells that distinguish active subsets: simulations for additional conditions. The top row shows the stochastic recruitment of individual cells. The bottom row is the proportion of cells with a different state (recruited versus not, i.e. place versus silent) for each pair of environment sizes. The first two conditions (left 2 columns) are the gamma-Poisson and equal-rate-Poisson models shown in Fig. 4C. To illustrate, the two arrows in the recruitment plot for the gamma-Poisson condition indicate the two environments (each given by a vertical line) compared at the intersection of the dotted lines in the plot below. The equal-rate-Poisson with lower and higher rates (right 2 columns) show that the distribution of the proportion of cells distinguishing active subsets is poor over a large range of equal-rate-Poisson conditions when each is compared to the gamma-Poisson condition. The equal-rate-Poisson low rate condition performs poorly for small environments, both for the number of cells distinguishing active subsets as well as for having many fewer cells with any fields to code the space. The equal-rate-Poisson high rate condition has an almost zero proportion of cells distinguishing active subsets in between larger environments since all cells are recruited.

Full References

1. W. B. Scoville, B. Milner, Loss of recent memory after bilateral hippocampal lesions, *J. Neurol. Neurosurg. Psychiatr.* **20**, 11–21 (1957).
2. J. O'Keefe, L. Nadel, *The Hippocampus as a Cognitive Map* (Oxford Univ. Press, Oxford, 1978).
3. R. Q. Quiroga, L. Reddy, G. Kreiman, C. Koch, I. Fried, Invariant visual representation by single neurons in the human brain., *Nature* **435**, 1102–7 (2005).
4. H. Gelbard-Sagiv, R. Mukamel, M. Harel, R. Malach, I. Fried, Internally generated reactivation of single neurons in human hippocampus during free recall, *Science* **322**, 96–101 (2008).
5. L. T. Thompson, P. J. Best, Place cells and silent cells in the hippocampus of freely-behaving rats, *J. Neurosci.* **9**, 2382–2390 (1989).
6. M. A. Wilson, B. L. McNaughton, Dynamics of the hippocampal ensemble code for space, *Science* **261**, 1055–1058 (1993).
7. S. Leutgeb, J. K. Leutgeb, A. Treves, M.-B. Moser, E. I. Moser, Distinct ensemble codes in hippocampal areas CA3 and CA1, *Science* **305**, 1295–1298 (2004).
8. J. O'Keefe, J. Dostrovsky, The hippocampus as a spatial map. Preliminary evidence from unit activity in the freely-moving rat, *Brain Res.* **34**, 171–175 (1971).
9. X. Liu, S. Ramirez, P. T. Pang, C. B. Puryear, A. Govindarajan, K. Deisseroth, S. Tonegawa, Optogenetic stimulation of a hippocampal engram activates fear memory recall, *Nature* **484**, 381–385 (2012).
10. M. P. Karlsson, L. M. Frank, Network dynamics underlying the formation of sparse, informative representations in the hippocampus, *J. Neurosci.* **28**, 14271–14281 (2008).
11. D. E. Davis, J. T. Emlen, A. W. Stokes, Studies on home range in the brown rat, *J. Mammal.* **29**, 207–225 (1948).
12. A. A. Fenton, H.-Y. Kao, S. A. Neymotin, A. Olypher, Y. Vayntrub, W. W. Lytton, N. Ludvig, Unmasking the CA1 ensemble place code by exposures to small and large environments: more place cells and multiple, irregularly arranged, and expanded place fields in the larger space, *J. Neurosci.* **28**, 11250–11262 (2008).
13. T. J. Davidson, F. Kloosterman, M. A. Wilson, Hippocampal replay of extended experience, *Neuron* **63**, 497–507 (2009).
14. K. B. Kjelstrup, T. Solstad, V. H. Brun, T. Hafting, S. Leutgeb, M. P. Witter, E. I. Moser, M.-B. Moser, Finite scale of spatial representation in the hippocampus, *Science* **321**, 140–143 (2008).
15. S. A. Hollup, S. Molden, J. G. Donnett, M. B. Moser, E. I. Moser, Accumulation of hippocampal place fields at the goal location in an annular watermaze task, *J. Neurosci.* **21**, 1635–1644 (2001).
16. Y. Ziv, L. D. Burns, E. D. Cocker, E. O. Hamel, K. K. Ghosh, L. J. Kitch, A. El Gamal, M. J. Schnitzer, Long-term dynamics of CA1 hippocampal place codes, *Nat. Neurosci.* **16**, 264–266 (2013).
17. O. Lundberg, *On Random Processes and Their Application to Sickness and Accident Statistics* (Almqvist & Wiksells, Uppsala, 1940).
18. M. Greenwood, G. U. Yule, An Inquiry into the Nature of Frequency Distributions Representative of Multiple Happenings with Particular Reference to the Occurrence of Multiple Attacks of Disease or of Repeated Accidents, *Journal of the Royal Statistical Society* **83**, 255 (1920).
19. J. Epsztein, M. Brecht, A. K. Lee, Intracellular determinants of hippocampal CA1 place and silent cell activity in a novel environment, *Neuron* **70**, 109–120 (2011).
20. D. Lee, B.-J. Lin, A. K. Lee, Hippocampal place fields emerge upon single-cell manipulation of excitability during behavior, *Science* **337**, 849–853 (2012).
21. T. Jarsky, R. Mady, B. Kennedy, N. Spruston, Distribution of bursting neurons in the CA1 region and the subiculum of the rat hippocampus, *J. Comp. Neurol.* **506**, 535–547 (2008).

22. E. J. Henriksen, L. L. Colgin, C. A. Barnes, M. P. Witter, M.-B. Moser, E. I. Moser, Spatial representation along the proximodistal axis of CA1, *Neuron* **68**, 127–137 (2010).
23. K. Mizuseki, K. Diba, E. Pastalkova, G. Buzsáki, Hippocampal CA1 pyramidal cells form functionally distinct sublayers, *Nat. Neurosci.* **14**, 1174–1181 (2011).
24. M. Tsodyks, T. Sejnowski, Associative memory and hippocampal place cells, *Int. J. Neural. Syst.* **6**, 81–86 (1995).
25. T. Hartley, N. Burgess, C. Lever, F. Cacucci, J. O’Keefe, Modeling place fields in terms of the cortical inputs to the hippocampus, *Hippocampus* **10**, 369–379 (2000).
26. T. Solstad, E. I. Moser, G. T. Einevoll, From grid cells to place cells: A mathematical model, *Hippocampus* **16**, 1026–1031 (2006).
27. G. Dragoi, S. Tonegawa, Preplay of future place cell sequences by hippocampal cellular assemblies, *Nature* **469**, 397–401 (2011).
28. G. Buzsáki, K. Mizuseki, The log-dynamic brain: how skewed distributions affect network operations, *Nat. Rev. Neurosci.* **15**, 264–278 (2014).
29. H. S. Milner-Brown, R. B. Stein, R. Yemm, The orderly recruitment of human motor units during voluntary isometric contractions, *J Physiol* **230**, 359–370 (1973).
30. M. A. Muniak, S. Ray, S. S. Hsiao, J. F. Dammann, S. J. Bensmaia, The neural coding of stimulus intensity: linking the population response of mechanoreceptive afferents with psychophysical behavior, *J. Neurosci.* **27**, 11687–11699 (2007).
31. A. J. Silva, Y. Zhou, T. Rogerson, J. Shobe, J. Balaji, Molecular and cellular approaches to memory allocation in neural circuits, *Science* **326**, 391–395 (2009).
32. G. Paxinos, C. Watson, *The Rat Brain in Stereotaxic Coordinates* (Elsevier Academic Press, San Diego, 5th Edition, 2005).
33. M. Karlsson, MatClust - File Exchange - MATLAB Central (2013) (available at <http://www.mathworks.com/matlabcentral/fileexchange/39663-matclust>).
34. N. Schmitzer-Torbert, J. Jackson, D. Henze, K. Harris, A. D. Redish, Quantitative measures of cluster quality for use in extracellular recordings, *Neuroscience* **131**, 1–11 (2005).
35. B. L. McNaughton, C. A. Barnes, J. O’Keefe, The contributions of position, direction, and velocity to single unit activity in the hippocampus of freely-moving rats, *Exp. Brain Res.* **52**, 41–49 (1983).
36. Y. Benjamini, Y. Hochberg, Controlling the false discovery rate: a practical and powerful approach to multiple testing, *Journal of the Royal Statistical Society. Series B (Methodological)* , 289–300 (1995).
37. H. W. Lilliefors, On the Kolmogorov-Smirnov Test for the Exponential Distribution with Mean Unknown, *Journal of the American Statistical Association* **64**, 387–389 (1969).
38. J. Grandell, *Mixed Poisson Processes* (CRC Press, 1997).
39. N. L. Johnson, A. W. Kemp, S. Kotz, *Univariate Discrete Distributions* (Wiley-Interscience, Hoboken, N.J, 3rd edition., 2005).
40. N. L. Johnson, S. Kotz, N. Balakrishnan, *Continuous Univariate Distributions, Vol. 1* (Wiley-Interscience, New York, 2nd Edition., 1994).